



Recycling and rheology of poly(lactic acid) (PLA) to make foams using supercritical fluid



Cite as: Phys. Fluids **33**, 067119 (2021); <https://doi.org/10.1063/5.0050649>

Submitted: 17 March 2021 . Accepted: 24 May 2021 . Published Online: 29 June 2021

 Lilian Lin,  Young Lee, and Heon E. Park (박희언)

COLLECTIONS



This paper was selected as Featured



View Online



Export Citation



CrossMark

Physics of Fluids

SPECIAL TOPIC: Tribute to
Frank M. White on his 88th Anniversary

SUBMIT TODAY!

Recycling and rheology of poly(lactic acid) (PLA) to make foams using supercritical fluid

Cite as: Phys. Fluids **33**, 067119 (2021); doi: [10.1063/5.0050649](https://doi.org/10.1063/5.0050649)

Submitted: 17 March 2021 · Accepted: 24 May 2021 ·

Published Online: 29 June 2021



Lilian Lin,  Young Lee,  and Heon E. Park (박희언)^{a)}

AFFILIATIONS

Department of Chemical and Process Engineering, University of Canterbury, Christchurch 8041, New Zealand

^{a)} Author to whom correspondence should be addressed: heon.park@canterbury.ac.nz

ABSTRACT

Biodegradable plastics are thought to be the possible directions in managing plastic pollutions. Unfortunately, they are not recycled in most countries since they are designed to decompose even though recycling is a more pragmatic method than landfill or incineration. Thus, it is more constructive to develop methods to recycle biodegradable plastics or to develop biodegradable yet recyclable plastics. In this study, we used cutlery with a composite of poly(lactic acid) (PLA) and talc. The possibility to recycle it to make foams was studied even though it will have lowered mechanical strength from the recycling process as it is less significant for this product. Tensile properties of solid PLA and foams showed no significant decrease in the strength up to three processes of compression molding and foaming. We performed shear rheometry to determine the thermal stability and dependences of the complex viscosity on frequency and temperature. The magnitude of the complex viscosity dramatically increased with decreasing frequency and such an upturn increased with temperature, but time-temperature superposition was valid at high temperatures. The extensional rheometry showed no strain hardening, but physical foaming using supercritical carbon dioxide (CO₂) could still occur, and the operating conditions to obtain various foamed structures were determined. We also compared the effects of one-directional against three-dimensional expansion. Overall, the concentration of CO₂ in PLA and crystallinity of the foams are the two key variables to describe the bulkiness of foams. Surprisingly, the lower the CO₂ concentration, the bulkier the foams at any sorption temperature and pressure.

Published under an exclusive license by AIP Publishing. <https://doi.org/10.1063/5.0050649>

I. INTRODUCTION

Synthetic polymers, i.e., plastics and rubbers, have been providing us benefits, such as hygiene, safety, functions, and convenience. Thus, we cannot imagine our lives without them. However, we have minimal knowledge regarding what to do after their lifecycle.^{1,2} Currently, plastics are not only contaminating our food sources but also threatening the whole ecosystem.³ The COVID-19 pandemic has clearly shown that we cannot live without plastics,^{4,5} especially disposable ones. It is scandalous that approximately half the production of plastics is used for single-use applications.⁶ We are now consuming these more than ever before,⁷ and the environmental issues will become even more drastic. Unfortunately, we are not ready to deal with all the polymer wastes that are disposed intentionally or accidentally. All those issues arise from the non-biodegradability of plastics. Plastics can be fragmented but not completely decomposed into simpler molecules.⁸

Today, biodegradable plastics provide a possible solution to prevent those issues.^{9,10} However, biodegradable plastics are not recycled in most countries, including New Zealand, since those are designed to degrade, i.e., break down, compromising mechanical strength, and

thus those should be disposed of in regular garbage bins. This is practiced by applying materials with a recycling code number of 7 (OTHER). For example, cutlery made of biodegradable plastics eventually end up in either landfill or energy recovery. One of the main reasons why biodegradability has been introduced to the plastic industry is to minimize adverse impacts on the environment due to disposals. It is an irony that the end of life of those is either landfill or burning rather than recycling, which is a much better treatment. Thus, it would be more constructive to develop methods to recycle biodegradable plastics or develop recyclable biodegradable plastics. If recyclable plastics degrade during physical recycling, that should be more expected for biodegradable plastics during physical recycling. For example, it does not seem to be a practical or favorable approach to recycle biodegradable cutlery back into cutlery due to lowered strength after recycling. Hence, it is reasonable to only consider recycling biodegradable cutlery in the applications where its mechanical strength is less significant. It is challenging to recycle one plastic product to another application because each product is made of a grade specifically suitable for each application.

We have chosen cutlery made of poly(lactic acid) or polylactide (PLA) to study the possibility of recycling it to make foams, as mechanical strength is not crucial, and defining the process windows. PLA is a thermoplastic aliphatic polyester which can be obtained by polymerizing derivatives from biomasses, such as cornstarch, sugarcane, and other wastes. PLA is the most successfully adopted synthetic bio-based plastic in the industry and research for applications, including three-dimensional (3D) printing, fabrics, packaging/bottles, films, automotive, electronics, and tissue engineering.¹¹ Moreover, its properties are similar to various non-degradable plastics. Approximately more than 200 000 patents have currently been published,¹² and this polymer is still actively studied. The number of relevant publications increases exponentially, such as for phase and stereocomplex behavior,^{13–16} rheology,^{17–20} foaming,^{21–25} and recycling.^{26–28} In addition, there are a significant number of reviews and monographs^{11,12,29–42} that are available.

First, we obtained rheological properties of PLA cutlery which are readily available in a local supermarket and were used as a model of biodegradable plastic. Linear viscoelastic (LVE) and extensional properties were used to determine the thermal stability, viscosity, strain hardening, and effect of temperature on rheological properties. We also studied the effect of the number of recycling processes on the mechanical strength of solid PLA.

We employed supercritical fluid (SCF) to physically foam the PLA cutlery rather than chemical foaming to avoid using any toxic chemicals. Detailed aspects of PLA foaming can be found elsewhere.⁴⁰ We have chosen supercritical carbon dioxide (SC-CO₂) as a physical blowing agent to foam PLA cutlery. Additionally, we performed foaming without adding any additives, such as chain extenders or thermal stabilizers. The studied PLA cutlery was made of an injection molding grade, which means it is a linear polymer, and did show strain hardening behavior, which is believed to be necessary for extending polymers in extensional rheometry, and it is challenging to foam. However, Weingart *et al.*⁴³ recently showed that strain hardening is not the only key parameter to achieve low density foams and they argued that slow crystallization can lead to a low foam density even without strain hardening. We performed foaming at relatively low pressure drop rates (PDRs) (hoping slow crystallization) to achieve various foamed structures at selected temperatures, pressures, and pressure drop rates.

We determined the effects of temperature, pressure, and pressure drop rate on the foamed structure, such as crystallinity, density, specific volume, cell (bubble) population density, and cell size to ensure it is possible to foam PLA cutlery to various foam structures for different applications. We also studied the effect of the expansion direction by comparing one-dimensional (1D) and three-dimensional (3D) expansion to account for different foaming situations. This comparison can be a guidance to predict the foaming behavior when there are dimensional constraints during foaming.

II. EXPERIMENTAL

A. Materials

We used carbon dioxide (CO₂, BOC Gas & Gear, New Zealand, >99.8% purity) as a physical blowing agent, nitrogen (N₂, BOC Gas & Gear, New Zealand, >99.99% purity, instrument grade) to make oxygen-free environment for the differential scanning calorimetry (DSC), thermogravimetric analysis (TGA), and rheometry, and helium

(BOC Gas & Gear, New Zealand, >99.8% purity, instrument grade) for pycnometry.

We have chosen disposable cutlery, which is a commercially available product (BioPak, New Zealand), as a model plastic product to be recycled into foams. The cutlery was made of poly(lactic acid) (Zhejiang Hisun Biomaterials Co., China), which is an injection molding grade. This grade has a composite of linear PLA with 25 wt. % of talc (diameter: 5–10 μm), which was added to increase the thermal resistance, flame retardance,^{44–46} and mechanical strength.^{46,47} The talc content was determined by a burn-off test. A piece of raw PLA cutlery was placed in a dried porcelain crucible, and then this crucible is placed in a furnace at 500 °C for 2 h. The talc content was determined from the residue amount assuming that there is no ash content other than talc. Liu *et al.*⁴⁸ reported that the composition of talc will change above 200 °C, but its weight loss between 100 and 800 °C is below 0.5%. Hence, we assume that the burn-off test does not underestimate the talc content. The melt flow rate of PLA/talc composite (i.e., cutlery) at 2.16 kg is 8–20 g per 10 min at temperature (T) = 190 °C and, the Vicat softening temperature is higher than 95 °C, and the Izod impact strength is higher than 2.5 kJ/m². The neat PLA component had been synthesized using one enantiomer, L-lactic acid, and the content of D-lactic acid was controlled to be below 1%. Its number average molecular weight (M_n) is 110 000 g/mol, weight average molecular weight (M_w) is 210 000 g/mol,⁴⁹ thus the polydispersity index (PDI) is 1.9.

B. Solubility and diffusivity of CO₂ in polymer

We should foam polymer only after saturating that with CO₂ to study the effect of concentration of CO₂ on foam properties. Otherwise, foaming during the transient sorption can lead to unknown concentration of CO₂. For this purpose, the solubility and diffusivity of CO₂ in PLA are necessary. Both data sets were obtained from literature sources and calculation. Data based on CO₂ sorption in PLA around room temperature^{50–53} and above its melting temperature^{54,55} are available. Li *et al.*⁵⁴ reported the solubility and diffusivity of CO₂ in PLA at various sorption pressures up to 28 MPa and temperatures at 180 and 200 °C. Since it was not possible⁵⁶ to obtain true solubility solely by either conventional weight change measurements or theories, Li *et al.*⁵⁴ used equations of state (EOS): the Sanchez–Lacombe (SL)^{54,56–59} and the Simha–Somcynsky (SS)^{54,60–62} models along with their apparent (i.e., without considering the buoyancy change due to swelling of polymer) solubility data. They reported model fitting parameters for both EOSs. Meanwhile, Li *et al.*⁶³ and Sarikhani *et al.*⁶⁴ used a visualization system⁶⁵ to obtain the volume swelling due to CO₂ absorption in polymers, and they could obtain the true solubility of CO₂ without any assistance of an EOS concluding that the SS model along with apparent data is similar to their solubility data with the combined visual and weight-measurement methods. Mahmood *et al.*⁵⁵ also argued that the SS model is a better choice for copolymers of L-lactide and D-lactide. Thus, we obtained the solubility values for pressures used in this study by interpolation using data by Li *et al.*⁵⁴ at 180 °C and those by Sarikhani *et al.*⁶⁴ up to 12 MPa at 140 and 160 °C. The solubility at 20 and 28 MPa at 140 and 160 °C was estimated by SS model calculations based on the method and parameters reported by Li *et al.*⁵⁴ Detailed methods can be found in the above literatures. One of the key parameters in predictions using an EOS is a set of the interaction parameters for mixing of two materials. While those are a

strong function of temperature in SL model predictions, those are temperature invariant⁵⁴ or a weak function of temperature⁵⁵ in SS model predictions. Thus, the same interaction parameters were used at 140 and 160 °C as reported values at 180 °C.⁵⁴ Mahmood *et al.*⁵⁵ showed that the content of D-lactide has little effect on the solubility and diffusivity of CO₂ in PLA, and the very low content of D-lactide in our sample should thus have no effect. The heterogeneity of the composite should not affect the solubility of CO₂ but could affect the CO₂ diffusion.⁶⁶ However, we assumed that the talc content does not affect the CO₂ diffusivity, and this assumption is valid based on the foamed structure (see Sec. III 3). The resulting values are shown in Table I.

Li *et al.*⁵⁴ reported the diffusivity of CO₂ in PLA at 180 and 200 °C are a very weak function of pressure. It is obvious that the diffusivity decreases with decreasing temperature, but those at 140 and 160 °C are not available in literature. An Arrhenius type of fitting model⁶⁷ was used, and parameters were obtained using the following expression and data (average over pressure) available:

$$\ln \frac{D(T)}{D(T_0)} = \frac{-E_{a,D}}{R} \left(\frac{1}{T} - \frac{1}{T_0} \right), \quad (1)$$

where $D(T)$ is the diffusivity at temperature T , T_0 is a reference T , R is the gas constant, and $E_{a,D}$ is the activation energy for the diffusion process and found to be 17.1 kJ/mol. Table II shows the estimated (140 and 160 °C) and average (180 °C) diffusivity of CO₂ in PLA. The saturation time will be estimated based on those values later in this paper. The accuracy of the diffusivity is not as crucial as the solubility since the full saturation can also be confirmed by the evenness of the foam structure.

C. Sample preparation

The raw PLA cutlery, molded solid, and foam samples were placed in a vacuum oven at room temperature more than two weeks before going through any experimental processes and tests. This procedure is to evaporate oxygen and any volatile chemicals including moisture and unreacted monomers present in those materials^{68–72} except for thermogravimetric analysis, where raw and unvacuumed PLA cutlery was used. The moisture or volatility level was determined using a moisture analyzer (Sartorius MA35, Germany) and was measured to be 0.3 wt. % after drying in the vacuum oven.

The handle of a PLA fork was cut to obtain the following dimensions of 7 (W) × 60 (L) × 1.3 mm (T) for tensile test.

For all other tests, compression-molded PLA was used. Prior to compression molding, the PLA cutlery and foams were cut into chip sized pieces that were smaller than 5 mm and crushed, respectively. Those chips were placed in a 130 (W) × 130 (L) × 1 mm (T) mold and shaped into be a plate via using compression molding in a hot

TABLE I. Solubility of CO₂ in PLA. Units are g CO₂/g PLA.

P (MPa)	140 °C	160 °C	180 °C
10	0.12	0.076	0.066
12	0.15	0.090	0.078
20	0.25	0.15	0.13
28	0.32	0.21	0.19

TABLE II. Diffusivity of CO₂ in PLA at various temperatures and the estimated saturation time.

	140 °C	160 °C	180 °C
Diffusivity (cm ² /s)	7.24×10^{-6}	1.25×10^{-6}	2.05×10^{-6} (Ref. 54)
Saturation time (min) for 1.5 mm thick disk	31	18	11

press (model 3912, Carver, Inc., USA). The operating conditions were 5 tons of compression force and at $T = 190$ °C. Once the sample was compressed, the hot press was cooled down with flowing water at a cooling rate of 30 °C/min. The compression-molded plate was cut into 25 mm diameter and 1 mm thickness disk shapes for rotational rheometry, 13 (W) × 18 mm (L) strips for extensional rheometry, 10 (W) × 60 mm (L) strips for tensile tests, and 25 mm diameter and 1.5 mm thickness disk shapes for foaming experiments.

D. Thermogravimetric analysis

A thermogravimetric analyzer (TGA, NETZSCH STA449 F3 Jupiter, Germany) was used to determine thermal decomposition of raw PLA cutlery, via its weight change due to heating up from 23 to 500 °C at 10 °C/min with nitrogen flow at 50 ml/min. Meanwhile, weight changes were recorded.

E. Differential scanning calorimetry

A differential scanning calorimeter (DSC, DSC8000, Perkin-Elmer, USA) was used to determine the phase transition behavior of the following three samples: raw fork, compression-molded plate, and foam which was obtained by operating CO₂ at $T = 180$ °C and $P = 10$ MPa with a normalized pressure drop rate (NPDR) [Eq. (11)] of 0.06 s⁻¹. Initially, a heating scan was implemented for each type of the stated samples at a temperature rate of 20 °C/min and the heating was from 35 to 255 °C to not only obtain the glass transition temperature and melting behavior but to also confirm whether the samples have any stereocomplexity. For all other foam samples obtained at various foaming conditions, a heating scan from 35 to 200 °C was implemented to attain their glass transition temperature and melting behavior. Figure 7 shows the following properties that were determined. The glass transition temperature (T_g) is the temperature at local maximum heat flow which was observed to be around 60 °C. The peak melting temperature ($T_{m,peak}$) is the temperature of the local maximum heat flow during the heating scan while the onset melting temperature ($T_{m,onset}$) is the temperature where the peak starts to develop from the baseline,⁷³ and the end melting temperature ($T_{m,end}$) is the temperature where the peak ends back to the baseline. In addition, the degree of crystallinity of every sample was determined using

$$\chi_c \equiv \frac{\Delta H_m}{(1 - \phi) \times \Delta H_{m,100\%}}, \quad (2)$$

where ϕ is the weight fraction of talc, which is 0.25 for this study, ΔH_m is the melting enthalpy of PLA which is obtained from the area under the curve of the melting peak (J/g), and $\Delta H_{m,100\%}$ is the melting

enthalpy of PLA with 100% crystallinity, which is 93.7 J/g at the equilibrium melting point.²⁹

F. Rotational shear rheometry

Linear viscoelasticity (LVE) or shear rheological properties and thermal stability were determined by SR5000 rotational rheometer (Rheometric Scientific, USA) with parallel disks of a 25 mm diameter and with a sample thickness of 1 mm at various temperatures. All tests were performed in a nitrogen environment to produce an oxygen-free environment. To minimize the effect of inertia, an inertia correction⁷⁴ for the upper plate was used. The thermal stability was determined at a frequency (ω) of 10 rad/s and a strain (γ) of 0.5% at 210 °C. Meanwhile, the storage $G'(\omega, t)$ and loss moduli $G''(\omega, t)$ were determined every 20 s. The change of the magnitude of complex viscosity (simply “the complex viscosity” for the rest of this study) with time (t) was used to determine the thermal stability,

$$|\eta^*(\omega, t)| \equiv \sqrt{\left[\frac{G'(\omega, t)}{\omega}\right]^2 + \left[\frac{G''(\omega, t)}{\omega}\right]^2}. \quad (3)$$

The complex viscosity with time was fitted to a linear equation. All the tests including foaming were performed within the determined time-frame where $|\eta^*(\omega, t)|$ is 10% less than its initial value. Saeidlou *et al.*¹⁵ preheated their stereocomplex PLA to 240 °C prior to rheological measurements at 180 °C to eliminate the previous stereocomplexity. However, the main goal of this study is understanding how to recycle PLA products, and this hardly involves such preheating in actual applications so the samples in this study were not preheated. Ultimately, all the D-content in the PLA sample in this study is relatively low; hence, stereocomplexity was not a concern.

To perform frequency sweep tests within the linear regime, i.e., linear viscoelasticity (LVE) data, strain sweep tests were initially performed. The maximum strains were determined by selecting the highest strain value before $|\eta^*(\omega, t)|$ starts decreasing with increasing strain at 100 rad/s. A strain of 0.5% was found to be the maximum strain at $T = 180$ °C to give LVE data. At higher temperatures, data should be in the linear regime at the same strain since less stress will be applied to the sample. Frequency sweep tests were performed at the strain of 0.5% to determine $G'(\omega, T)$, $G''(\omega, T)$, and $|\eta^*(\omega, T)|$, where T is the test temperature of 180, 190, 200, and 210 °C, and at decreasing frequency between 100 and 0.01 rad/s. Data with torque values below the instrument limitation were not reported.

G. Extensional rheometry

Extensional rheometry was performed using a Sentmanat Extensional Rheometer (SER, model SER-HV-A01, Xpansion Instruments, USA)^{75,76} and an Advanced Rheometric Expansion System (ARES, Rheometric Scientific, USA) to determine the tensile stress growth function $\eta_E^+(\dot{\epsilon}, t)$ of PLA at $T = 180$ °C. All tests were performed in a nitrogen environment to produce an oxygen-free environment. A sample was loaded on the vertically standing two drums at $T = 180$ °C. After a certain soaking time at the test temperature, the ARES motor started rotating the drums of SER and stretched the sample at a constant Hencky strain rate ($\dot{\epsilon}$)

$$\dot{\epsilon} = 2\Omega R_D / L_0, \quad (4)$$

where Ω is the rotational speed of ARES motor (rad/s), R_D is the drum radius (0.5155 cm), and L_0 is the fixed length of the sample (1.272 cm), i.e., the distance between the two drums. Meanwhile, the torque (M) necessary for the rotating drums was recorded.

The sample dimensions were measured at ambient temperature (normally 20 °C) prior to loading to SER. Thus, those during a test should be estimated after accounting for the changes in the cross-sectional area, due to the thermal expansion⁷⁶ and stretching, which lead to the exponential decrease in the cross-sectional area with time at a constant Hencky strain rate. The transient cross-sectional area of the sample is then

$$A(\dot{\epsilon}, t) = A_0 \left(\frac{\rho_0}{\rho_T}\right)^{2/3} e^{-\dot{\epsilon}t} = W_0 H_0 \left(\frac{\rho_0}{\rho_T}\right)^{2/3} e^{-\dot{\epsilon}t}, \quad (5)$$

where t is elapsed time, ρ_T is the sample density at the test temperature, and ρ_0 , A_0 , W_0 , and H_0 are the density, cross-sectional area, width, and thickness of the solid sample determined at room temperature, respectively. The transient tensile stress is the ratio of the tensile force to the cross-sectional area,

$$\sigma^+(\dot{\epsilon}, t) = \frac{F(\dot{\epsilon}, t)}{A(\dot{\epsilon}, t)}, \quad (6)$$

where $F(\dot{\epsilon}, t)$ is the transient tensile force on the sample and can be obtained from the torque on the drum,

$$F(\dot{\epsilon}, t) = \frac{M(\dot{\epsilon}, t)}{2R_D}, \quad (7)$$

where $M(\dot{\epsilon}, t)$ is the torque measured by ARES. Finally, the tensile stress growth function (often wrongfully defined as extensional viscosity) is obtained by

$$\eta_E^+(\dot{\epsilon}, t) \equiv \frac{\sigma^+(\dot{\epsilon}, t)}{\dot{\epsilon}}, \quad (8)$$

and can be calculated by combining Eq. (5) through to Eq. (8),

$$\eta_E^+(\dot{\epsilon}, t) = \frac{M(\dot{\epsilon}, t)e^{\dot{\epsilon}t}}{2R_D W_0 H_0 \left(\frac{\rho_0}{\rho_T}\right)^{2/3}}. \quad (9)$$

We reported only data with torque above the instrumental limit and up to the time when the sample holding clamps of SER touch each other after a $3/4$ turn of the drums.

H. Tensile properties of solid PLA

Tensile properties of solid samples were determined by a universal test machine (UTM, model 5965, Instron, USA). All tests were performed at tensile speed of 50 mm/s at $T = 20$ °C. PLA is relatively brittle and not ductile; therefore, the data analysis was comparatively straightforward. Young's modulus is the slope of the stress vs strain curve. The tensile strength and elongation at break are the stress and strain, respectively, and at where the sample broke. The yield strength of PLA is the same as the tensile strength since no yielding or ductile behavior was found. Toughness is the area under the curve and the average was taken from six replicates.

I. Batch foaming

We used an environmentally benign foaming process to physically foam molded PLA disks using supercritical CO₂ in a batch foaming system. Even though CO₂ has a bad reputation in terms of global warming potential aspects, CO₂ shows the lowest global warming potential among physical blowing agents. It is also nontoxic and easy to recycle. Moreover, a decent amount of CO₂ can be absorbed by many types of polymers. The principle of physical foaming is simple. We dissolve supercritical CO₂ in PLA at a high pressure and temperature because more CO₂ can be dissolved at elevated pressure and we needed the molten state of polymer to make bulky foams. After saturating PLA with CO₂, a vent valve is promptly opened to induce a sudden drop in the pressure and thus the solubility of CO₂, which leads to bubbling. This process does not involve any chemical reaction of toxic chemicals; hence, it is not only environmentally benign but also nonhazardous.

1. Foaming system

The piping and instrumentation diagram (P&ID) for this batch foaming system is shown in Fig. 1. A high-pressure, foaming chamber (Series 4651, Parr Instrument Company, USA) was preheated to the desired sorption temperature using a ceramic band heater (TEMPCO, New Zealand). The temperature was controlled using a thermocouple and a temperature controller. Once the desired temperature was reached, a compression-molded PLA disk was placed into the foaming chamber and the system was evacuated for 5 min. Then, CO₂ was injected into the system from a CO₂ cylinder. The system was pressurized to the desired sorption pressure using a syringe pump (D260, Teledyne ISCO, USA). When the saturation of CO₂ sorption in the PLA sample was achieved, one out of the three vent valves was opened to induce pressure drop in the system and foaming. For vent valve 1 or 2, the pressure drop rate is controlled by the set gap of the pin valve, which was adjusted prior to CO₂ sorption. In addition to the size of

the gap of the pin valve(s), the length of the tubing will affect the flow of SC-CO₂,⁷⁷ and jet disintegration⁷⁸ may affect the release of SC-CO₂. Vent valve 1 is for the slowest pressure release.

The pressure drop rate (PDR) is often defined as the time derivative of pressure^{68,79,80}

$$\text{PDR} \equiv -\frac{dP}{dt}, \quad (10)$$

where P is the chamber pressure and t is the time. PDR decreases with time as can be seen in Fig. 2(a) so that no single value can be reported except for the initial value. To obtain a more proper definition of PDR, i.e., a single value, PDR can be normalized by pressure to give the pressure drop rate (NPDR),

$$\text{NPDR} \equiv -\frac{1}{P} \frac{dP}{dt} = -\frac{d(\ln P)}{dt}. \quad (11)$$

Thus, PDR is the magnitude of the slope of $\ln P$ vs t . The PDR at the beginning of depressurization can be also estimated by

$$\text{PDR}|_{t=0} = P_0 \left[-\frac{1}{P} \frac{dP}{dt} \right] = P_0 \times \text{NPDR}, \quad (12)$$

where P_0 is the initial pressure. Both PDR and NPDR were used in this study.

The two pin valves (vent valves 1 and 2) were adjusted at test pressures and temperatures without a sample and with/without the sample supporting fixture (Fig. 3), i.e., a blank run to give the designated NPDR values up on opening one of those vent valves. These NPDRs could be different with the same opening of the pin valves in tests with the sample and sample supporting fixture. However, Fig. 2(b) shows that there is no difference in the slope, i.e., the pressure drop for all the different methods is reproducible, up to 14 s. Trials with the sample supporting fixture for the accelerated diffusion methods (see Sec. II I 3) took less time to release the whole pressure from the

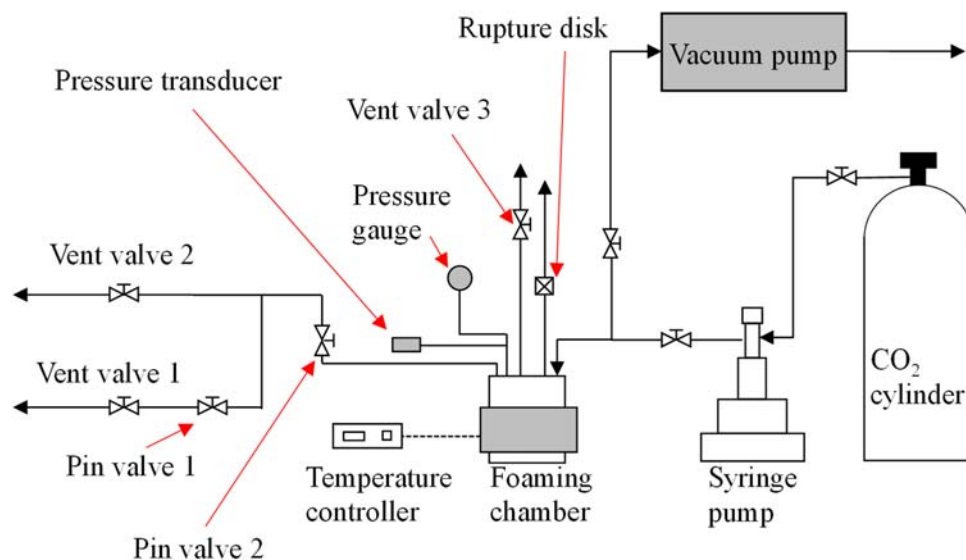


FIG. 1. Piping and instrumentation diagram for batch foaming process.

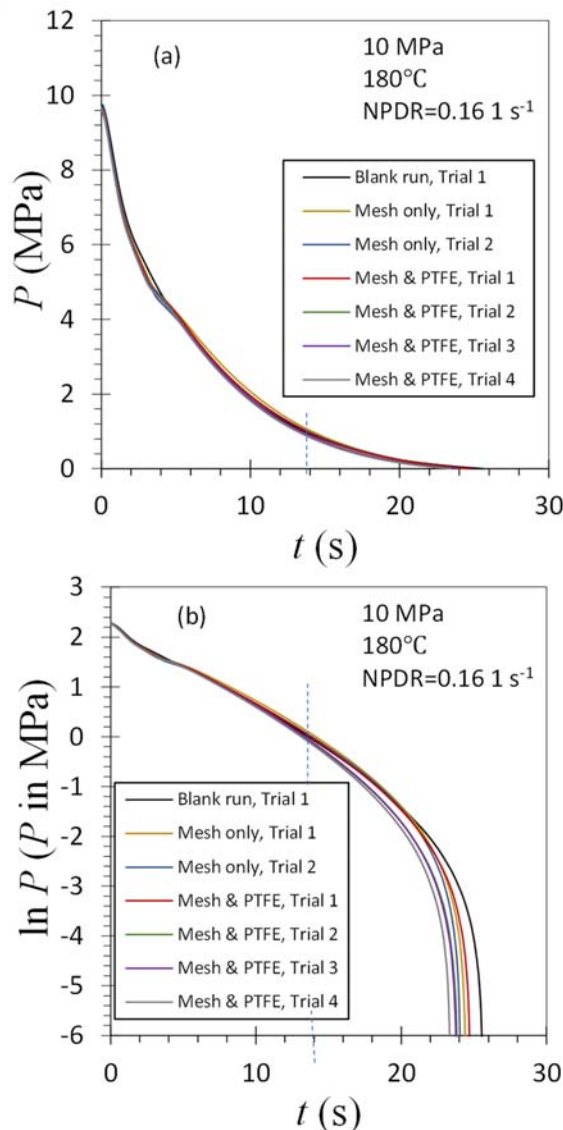


FIG. 2. Reproducibility of pressure release from $P = 10$ MPa and $T = 180^\circ\text{C}$ at various conditions inside the chamber. Blue dashed line indicates 14 s. Polytetrafluoroethylene (PTFE) is the coating on the woven glass fibers cylinder, (a) pressure with time and (b) $\ln P$ with time.

foaming chamber compared to the blank runs. This suggests that less amount of gas was present in the chamber due to the occupied volume by the fixture. However, in 14 s, the pressure dropped to only 10% of the initial value as shown in Fig. 2(a). The differential pressure over time, which is the driving force for foaming, became comparably small. In consequence, the difference in the total time to complete the chamber evacuation will not matter even with a sample inside the chamber. When the system is operated at the same NPDR, it takes the same time to complete a depressurization despite what the initial pressure and temperature were. Vent valve 3 was used to give the maximum PDR of the system. During

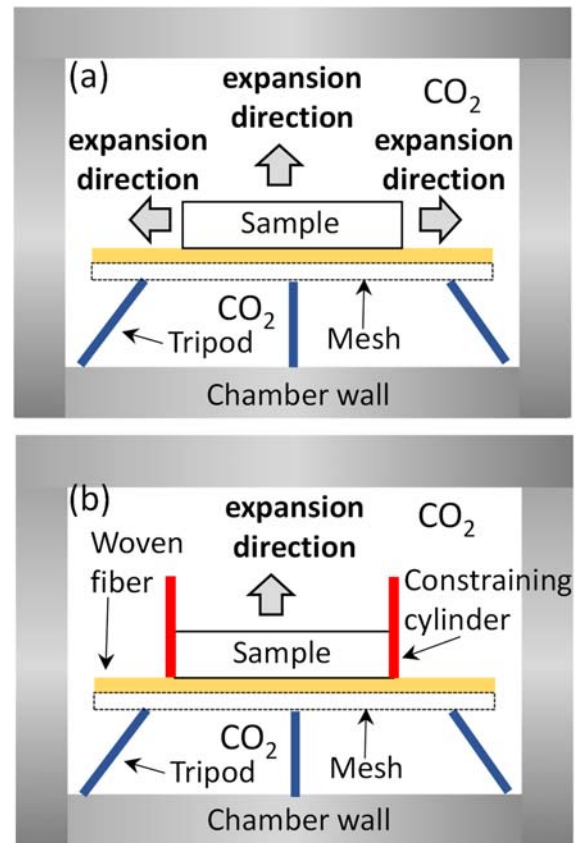


FIG. 3. Inner setup of the foaming chamber. (a) Sample loading for 3D foaming (sorption) and (b) sample loading with a constraining cylinder for 1D foaming (sorption) study. The sample supporting fixture is composed of a tripod, a stainless steel mesh, and loosely woven glass fibers coated with PTFE (images are not to scale).

depressurization, a pressure transducer was used to record the pressure profile every 0.001 s.

2. Foaming procedure and conditions

First, the chamber with the sample holding fixture was heated to a desired temperature, and then a sample was loaded on the fixture with or without the constraining cylinder. After closing the cover of the chamber, the chamber was evacuated for 5 min. The system was pressurized to a desired pressure using the syringe pump after filling the system with CO_2 . After soaking the sample for the estimated saturation time (see Sec. II 13), one of the vent valves was promptly opened to induce depressurization and thus foaming. The sample holding fixture (Fig. 3) was constructed to allow the bottom of the sample to be in contact with CO_2 . This fixture composed of a tripod, a coarse mesh made of stainless steel 316, and loosely woven glass fibers coated with polytetrafluoroethylene (PTFE). It was confirmed that the saturation with CO_2 was four times faster by placing the sample on top of the fixture instead of directly putting it on the chamber bottom.

In order to study the difference of one-dimensional (1D) vs three-dimensional (3D) expansion at various PDRs, samples were

loaded in two different ways shown in Fig. 3. For 1D expansion, the disk sample was placed on a fixture and in a constraining hollow cylinder. This cylinder was produced from woven glass fibers and coated with PTFE to prevent samples from sticking onto its surface.⁸¹ For 3D expansion, a disk sample was placed on the fixture without the constraining hollow cylinder. It should be noted that 3D expansion will be described as two-dimensional (2D), i.e., radial and longitudinal expansion in the cylindrical coordinate system.

The CO₂ sorption temperature and the pressure were set to $T = 180^\circ\text{C}$ and $P = 10\text{ MPa}$. As for foaming, it took place at three NPDRs which were 0.06, 0.13, and 0.16 s^{-1} . The average values of foam properties were taken from four replicates.

To study the effects of operating conditions (temperature, pressure, concentration of CO₂) on the foamed structure, sorption conditions were set to 140, 160, and 180°C and 10, 12, 20, and 28 MPa. Foaming took place at NPDR of 0.02 s^{-1} . Similarly to the above, the average values of foam properties were taken from four replicates.

3. Estimating time for saturation of solid with CO₂

The concentration of dissolved CO₂ should be controlled as it is one of the key variables in foaming study. One of the easiest approaches to tackle this control will be leaving the sample in the chamber at a given time. This will at least be after the time required for the concentration of CO₂ to reach its solubility in the polymer. To minimize thermal degradation, the sorption time should also be minimized. Thus, the estimation of saturation time is important. Park and Dealy⁵⁶ used the analytical solution of Fick's second law of diffusion to estimate the saturation time in Cartesian coordinates system since they saturated a rectangular sample. However, we used disk samples, so Fick's second law of diffusion in cylindrical coordinates system should be used,

$$\frac{\partial C}{\partial t} = \frac{D}{r} \left[\frac{\partial}{\partial r} \left(r \frac{\partial C}{\partial r} \right) + \frac{\partial}{\partial \theta} \left(\frac{1}{r} \frac{\partial C}{\partial \theta} \right) + \frac{\partial}{\partial z} \left(r \frac{\partial C}{\partial z} \right) \right], \quad (13)$$

where t is the elapsed time, C is the concentration of CO₂ in polymer, D is the diffusivity of CO₂ in polymer, which is assumed to be independent of C , r is the radial, θ is the angular, and z is the axial (longitudinal) coordinate variables in the cylindrical coordinates system. Since there should be no change of C in θ direction, Eq. (13) becomes

$$\frac{\partial C}{\partial t} = \frac{D}{r} \left[\frac{\partial}{\partial r} \left(r \frac{\partial C}{\partial r} \right) + \frac{\partial}{\partial z} \left(r \frac{\partial C}{\partial z} \right) \right]. \quad (14)$$

For 1D sorption (or expansion) [Fig. 3(a)], in which CO₂ sorption takes place only in z -direction, Eq. (14) can be reduced to

$$\frac{\partial C}{\partial t} = D \frac{\partial^2 C}{\partial z^2}. \quad (15)$$

The analytical solutions are shown in Appendixes A and B, which show the two different versions of solutions depending on how the boundary conditions were defined. The transient amount of CO₂ absorbed by polymer can be obtained by

$$M(t) = \int_0^h C(z, t) dz, \quad (16)$$

where h is the length of the path of CO₂ diffusing in polymer. Using the analytical solutions of Eq. (15), Eq. (16) becomes

$$\frac{M(t)}{M(\infty)} = 1 - \sum_{n=0}^{\infty} \frac{8}{(2n+1)^2 \pi^2} \exp\left(-\frac{D(2n+1)^2 \pi^2 t}{4h^2}\right), \quad (17)$$

where $M(\infty)$ is the amount of CO₂ absorbed by polymer after infinite sorption time and n is the summation index. For $M(t)/M(\infty) = 0.99$, which is considered saturation in this study, $Dt/h^2 = 1.64$.⁵⁶ As a result, the saturation time, i.e., the sorption time for saturating polymer with CO₂ can be calculated using

$$t_{\text{sat}} = \frac{1.64h^2}{D}. \quad (18)$$

Since we used the accelerated system in which sorption takes place not only from the top but also from the bottom of the sample, as shown in Fig. 3, h is half the thickness of the sample. It should be noted that the sample will swell up on sorption, so that the thickness varies with time. In order to obtain the saturation time, the final (ultimate) thickness of the sample needs to be determined. This is the volume swelling due to dissolved CO₂ at $P = 28\text{ MPa}$ and where the maximum swelling was obtained by applying the SS model prediction with experimental data.⁵⁴

For the case of 3D sorption (or expansion) [Fig. 3(b)], Eq. (14) should be solved, and Bessel function should be used in the analytical solutions which are truly more complicated than Eq. (17). Since there is another dimension for CO₂ sorption, the saturation time for 3D should be shorter than for 1D. Thus, it suggests that the saturation time obtained for 1D sorption is sufficient for 3D sorption and provides the same thermal history for both 1D and 3D foaming. Essentially, thin disks were used for foaming which denotes that the sorption in axial direction will dominantly saturate the polymer over the radial direction. In consequence, 3D sorption can also be approximated to 1D sorption. Table II shows the estimated saturation time for 1.5 mm in thickness disks. Foaming (i.e., depressurization) was performed after placing the sample in the chamber with CO₂ at given temperature to attain the saturation time. It was confirmed that there is no significant difference in the foamed structure between locations near the top and bottom surfaces and the center implying that the estimated saturation time was reasonable.

J. Density of solid and foam

The density of all unfoamed and foamed PLA samples was determined using a densitometer kit (YDK01, Sartorius, Germany) on a microbalance (CPA124S, Sartorius, Germany) utilizing the Archimedes principle (ISO 1183–1987). First, the foam sample was weighed in the air ($W_{\text{in air}}$) and then weighed after it was submerged in distilled water ($W_{\text{in W}}$). By finding all those masses, the density of the sample (ρ_0) can be determined using the equation below where ρ_W is the density of distilled water

$$\rho_0 = \frac{W_{\text{in air}} \rho_W}{W_{\text{in air}} - W_{\text{in W}}}. \quad (19)$$

The average density of the sample was calculated by acquiring the average from four measurement replicates.

The density of PLA/talc as a function of temperature is necessary to analyze both shear and extensional rheometry data. Sato *et al.*⁸² reported pressure-volume-temperature (PVT) data of neat PLA and fitting parameters for a modified cell model equation of state (MCM

EOS) developed by Dee and Walsh.^{83,84} It should be noted that the MCM EOS cannot be used to predict the density of PLA/talc alone, as this model requires the experimental data for its parameters. In addition, PLA/talc composite is used in our studies and no PVT data were published for that. Mehrjerdi *et al.*⁸⁵ showed that the density of polyethylene/talc linearly decreases with temperature, and its slope is invariant with the content of talc. This implies that the talc does not contribute to the density change of the composite with temperature. Assuming that the same rationale is valid, we shifted Sato *et al.*'s data vertically until this matches with the density of compression-molded PLA/talc ($T = 20^\circ\text{C}$), which was used for rheological measurements. The density of PLA/talc at high temperatures was extrapolated from the shifted curves that are observed in Fig. 4.

K. Cell (population) density and cell size of foams

To capture cell structures, foams were cut parallel to the axial (longitudinal) direction, i.e., vertical to the bottom surface to see the side view (vertical shape) of the cells and parallel to the bottom surface to see the top view of the cells (Fig. 5). Foams could be placed in liquid nitrogen prior cutting to prevent shear deformation. For our samples, those were not placed in liquid nitrogen since those were fairly brittle and could be cut without shearing the surface. The cut foams were sputter-coated with palladium using a sample preparation system (Q150T ES, Quorum Technologies, Canada) at a sputter current of 30 mA and sputter time of 60 s. A scanning electron microscope (SEM, JSM-IT300, JOEL, Japan) is used to capture 2D images of foamed structures.

The cell density, i.e., cell population per unit volume, can be conventionally determined from a 3D cross-sectional image of a foam sample as shown below by assuming that spherical cells are uniformly distributed in all directions,

$$\rho_{\text{cell}} = \left(\frac{n}{A}\right)^{3/2}, \quad (20)$$

where ρ_{cell} is the density of the cell, A is the area of the image of interest, and n is the number of cells in the area. However, we need to

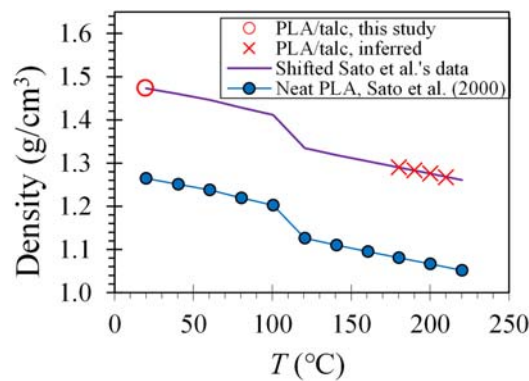


FIG. 4. Experimental densities of PLA at various temperatures and compression-molded PLA/talc at $T = 20^\circ\text{C}$. The density of PLA/talc at high temperature was gathered from the shifted Sato *et al.*'s data.⁸² The inferred densities at 20, 180, 190, 200, and 210°C are 1.472 (raw fork), 1.474, 1.290, 1.283, 1.276, and 1.267 g/cm^3 , respectively.

exclude the void volume contributed by cells in the control volume for the cell density calculation. The easiest method is using a correction factor (the volume expansion ratio) as the following equation:^{68,86,87}

$$\rho_{\text{cell}} \equiv \left(\frac{n}{A}\right)^{3/2}_{\text{foam}} \frac{V_{\text{foam}}}{V_{\text{solid}}} = \left(\frac{n}{A}\right)^{3/2}_{\text{foam}} \frac{\rho_{0,\text{solid}}}{\rho_{0,\text{foam}}}, \quad (21)$$

where V_{foam} is the volume of foam, and V_{solid} is the volume of solid sample without foaming, $\rho_{0,\text{solid}}$ is the density of solid, and $\rho_{0,\text{foam}}$ is the density of foam. This definition can help compare the density of the cell (ρ_{cell}) among the foams with different bulk volumes, since this shows the number of cells per unfoamed volume excluding void volume. Thus, the physical meaning of ρ_{cell} is also the cell-nucleus density at the beginning of the foaming process assuming that no coalescence^{88,89} or breakup^{90–92} occurred during foaming. The cell density was determined on two different locations of an SEM image of four replicates. The cell density is an important parameter as it can be related to the mechanical and bulk properties of the foam.

L. Cell circularity of foams

Cell properties (circularity, density, and diameter) were determined by using an image processing software, ImageJ using the SEM images of cell structures. The circularity of cells is defined by the following equation:

$$\text{Circularity} \equiv \frac{4\pi \text{Area}}{\text{Perimeter}^2}, \quad (22)$$

where Area is the cross-sectional area of a cell, and Perimeter is the perimeter of a cell. When a cell is circular, Circularity is unity. As for when this circularity term decreases, cell shape is polyhedral with decreasing number of vertices. When a cell is a line, this term is zero.

M. Void fraction and open cell contents

The volume of a foam (V_{foam}) can be obtained by

$$V_{\text{foam}} = \frac{m_{\text{foam}}}{\rho_{0,\text{foam}}}, \quad (23)$$

where m_{foam} is the mass of the foam sample assuming that air in the cells does not contribute to the foam mass, and is composed of three volumes,

$$V_{\text{foam}} = V_{\text{solid}} + V_{\text{closed}} + V_{\text{open}}, \quad (24)$$

where V_{solid} is the volume of the solid member which can be determined by

$$V_{\text{solid}} = \frac{m_{\text{foam}}}{\rho_{0,\text{solid}}}, \quad (25)$$

where V_{closed} is the volume of closed cells and V_{open} is the volume of open cells which was determined using a pycnometer (UltraFoam, Quantachrome Instruments, Austria) at $T = 20^\circ\text{C}$ based on ASTM D 6226 (Standard Test Method for Open Cell Content of Rigid Cellular Plastics) using helium at $P = 0.4$ bar. The volume of closed cells (V_{closed}) can be obtained by

$$V_{\text{closed}} = V_{\text{foam}} - (V_{\text{solid}} + V_{\text{open}}). \quad (26)$$

For the total cell (void) volume (V_{cell}) which is either occupied by CO_2 or air in the foam is expressed as

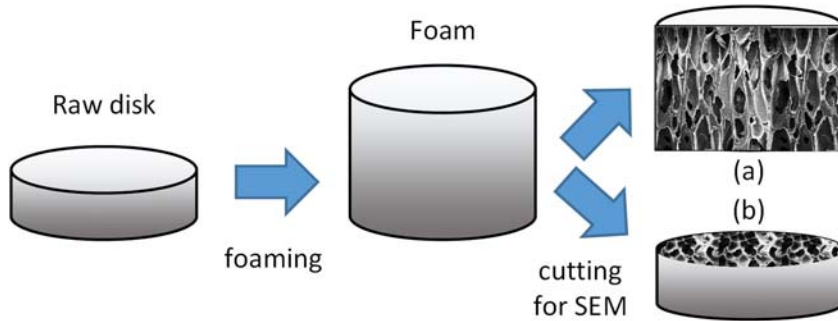


FIG. 5. Foam cutting for SEM images. (a) Orthogonal to the bottom surface and (b) parallel to the bottom surface. (Images are not to scale.)

$$V_{\text{cell}} = V_{\text{closed}} + V_{\text{open}} = V_{\text{foam}} - V_{\text{solid}}. \quad (27)$$

The degree of foaming can be determined by the cell (void) volume fraction (f_{cell}), which is denoted as

$$f_{\text{cell}} \equiv \frac{V_{\text{cell}}}{V_{\text{foam}}} = 1 - \frac{\rho_{0,\text{foam}}}{\rho_{0,\text{solid}}}. \quad (28)$$

Hence, the volume fraction of the solid (f_{solid}), closed cell (f_{closed}), and open cell contents (f_{open}) can be obtained, respectively, with the following:

$$f_{\text{solid}} = \frac{V_{\text{solid}}}{V_{\text{foam}}}, \quad (29)$$

$$f_{\text{closed}} = \frac{V_{\text{closed}}}{V_{\text{foam}}}, \quad (30)$$

$$f_{\text{open}} = \frac{V_{\text{open}}}{V_{\text{foam}}}. \quad (31)$$

N. Statistical analysis

Statistical analysis was performed by a one-sided student *t*-test using Microsoft Excel. We considered the statistical significance when the *p*-value was lower than 0.05. We marked two different significance levels as * for $p < 0.05$ and ** for $p < 0.01$. The number of replicates implemented is shown in the relevant sections.

III. RESULTS AND DISCUSSION

A. Thermal stability at high temperature

Thermal stability of raw PLA fork, which had not been dried, was determined by TGA measurements in a nitrogen environment. The two sets of weight change data with temperature are almost identical as shown in Fig. 6. The initial weight decreased by 1.5% is thought to be due to the moisture evaporation. The weight decreased immensely between 300 and 390 °C implying most of the organic components are decomposed to gases in that regime. The lowest weight percent stayed around 26% even after leaving the sample at 500 °C for hours (not shown in Fig. 6) and there was a dark-colored debris, i.e., an undecomposed organic material on the sample cubicle. This happened because there was the presence of talc that was holding the organic components together as it is commonly used as a flame retardant. The weight % of talc shown in TGA is slightly higher than the actual specified amount of talc. All those behaviors are similar

to what Jain *et al.*⁹³ reported for neat PLA and PLA with talc up to 5 wt. %.

B. Phase transition behaviors

Thermal behavior of three samples: raw fork, compression-molded plate, and foam foamed at $T = 180$ °C, $P = 10$ MPa, and $\text{NPDR} = 0.06 \text{ s}^{-1}$ were determined by DSC measurements. Figure 7 shows the glass transition and melting behaviors of the samples.

Table III shows the resulting transition temperatures and crystallinity. The melting behavior of the three samples is quite different implying that those had experienced very different cooling history after each molten process. The molded plate shows a bimodal melting peak, and the foam shows an even trimodal peak while the fork shows only a unimodal peak with a small shoulder. The phenomenon of peak splitting is similar to the case of stereocomplex PLA,^{14,15} but this is not the case as the D-lactic acid content in our sample is very low and no peak was found during the heating scan around $T = 250$ °C (not shown in Fig. 7). Jain *et al.*⁹³ reported a similar behavior for PLA/talc composites up to 5 wt. % of talc: The peak temperature ($T_{\text{m,peak}}$)

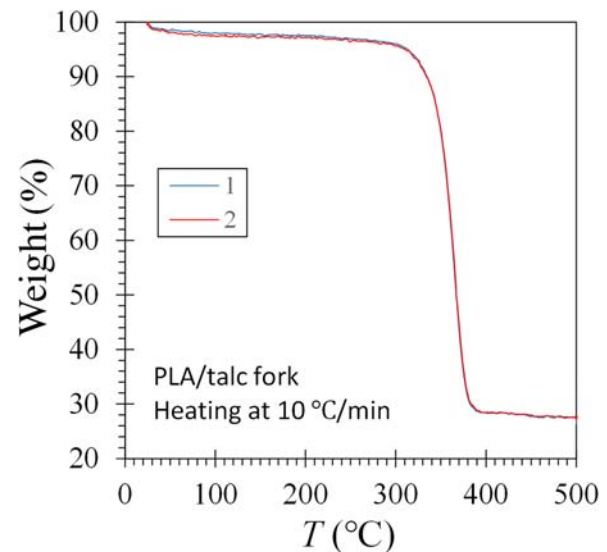


FIG. 6. Two distinct runs to show the weight change of PLA/talc cutlery during heating up at 10 °C/min.

TABLE III. Transition temperatures ($^{\circ}\text{C}$) and crystallinity (%) of raw fork, compression-molded plate, and foam foamed at $T = 180^{\circ}\text{C}$, $P = 10$ MPa, and NPDR = 0.06 s^{-1} . Heating and cooling rates were $20^{\circ}\text{C}/\text{min}$.

Sample	T_g	$T_{m,\text{onset}}$	$T_{m,\text{peak}}$	$T_{m,\text{end}}$	Crystallinity
Fork	66.2	145.0	154.4	163.3	31.5
Molded	66.2	150.6	161.7, 169.7	172.0	41.1
Foam	66.4	144.9	151.4, 161.0, 168.3	171.1	42.9

for neat PLA is 168°C , and the bimodal peak temperatures were 165 and 170°C for their PLA/talc composites. The behavior of bimodal melting peaks appeared because compounded talc particles led to two different crystalline structures. Considering that the cooling rate in the compression molding was $30^{\circ}\text{C}/\text{min}$, which was slow enough to induce phase separation leading to the bimodal melting peak, we can presume that the cutlery was cooled down much faster than $30^{\circ}\text{C}/\text{min}$. Consequently, the crystallinity of the fork is lower than the compression-molded plate.

A multi-mode of a melting peak was even more apparent with the foam. Unlike injection or compression-molding which involves quiescent crystallization, the foaming process involves significant elongation as a consequence of the alignment of both polymeric chains and talc network. Essentially, the latter seems to have contributed to the trimodal melting peak. All other foams also showed trimodal melting peaks as shown in Tables IV and V.

The end melting temperature ($T_{m,\text{end}}$) of 172°C for the compression-molded plate suggests that $T = 175^{\circ}\text{C}$ would be a very marginal temperature for rheometry since rheological tests at that temperature may cause shear-induced crystallization.^{94,95} Hence, $T = 180^{\circ}\text{C}$ was chosen as the lowest temperature for both shear and extensional rheometry. In spite of that, the lowest foaming temperature will be a different case. Foaming can still take place in a solid. Moreover, all polymer/ CO_2 can be molten at a considerably lower temperature than the melting temperature of the neat polymer due to plasticization. Therefore, $T = 140^{\circ}\text{C}$ was selected for the lowest foaming temperature. Nofar *et al.*⁹⁶ reported the melting temperature (T_m) of PLA linearly decreased by 12°C with increased CO_2 sorption pressure by 4.5 MPa. Considering the onset melting temperature for the compressed molded plate ($T_{m,\text{onset}}$) is 150.6°C , our PLA/talc sample saturated with CO_2 at $T = 140^{\circ}\text{C}$ and $P = 10$ MPa would be molten.

TABLE V. Transition temperatures ($^{\circ}\text{C}$) and crystallinity (%) of foams foamed at NPDR = 0.02 s^{-1} . Pressure is in MPa.

Sorption P	Sorption T	T_g	$T_{m,\text{onset}}$	$T_{m,\text{peak}}$	$T_{m,\text{end}}$	Crystallinity
10	140	62.8	160.5	154.6, 156.1, 167.6	172.7	36.1
	160	67.3	159.9	154.7, 157.5, 168.0	171.9	29.2
	180	65.3	153.2	142.8, 158.9, 167.7	172.8	43.2
20	140	66.4	164.1	156.4, 158.9, 168.2	171.7	32.7
	160	70.7	164.7	157.0, 160.0, 170.3	173.8	34.9
	180	64.4	162.2	154.2, 157.3, 168.1	171.8	32.2
28	140	68.0	164.8	156.8, 160.2, 169.4	172.5	32.5
	160	66.8	163.3	155.7, 158.6, 168.6	172.1	33.0
	180	64.8	162.3	155.0, 157.4, 168.2	172.5	34.7

TABLE IV. Transition temperatures ($^{\circ}\text{C}$) and crystallinity (%) of foams foamed at 1D and 3D expansion at $T = 180^{\circ}\text{C}$ and $P = 10$ MPa. NPDR in is s^{-1} .

	NPDR	T_g	$T_{m,\text{onset}}$	$T_{m,\text{peak}}$	$T_{m,\text{end}}$	Crystallinity
1D	0.06	64.7	157.4	146.2, 160.5, 168.3	171.4	43.1
	0.12	64.6	154.0	157.1, 167.4, 177.9	179.7	39.3
	0.16	62.5	154.8	146.5, 157.7, 167.3	171.2	39.1
3D	0.06	66.4	144.9	151.4, 161.0, 168.3	171.1	42.9
	0.12	65.4	154.5	135.2, 157.2, 166.8	169.7	39.8
	0.16	65.3	156.8	142.8, 159.6, 167.6	171.2	39.6

Glass transition temperature (T_g) appeared somewhere between 60 and 71°C where an overshoot (local maximum) was observed, and such a behavior has also been reported.⁹⁷ The glass transition temperatures are similar in which Nofar *et al.*⁹⁸ reported for PLA with 4.6 mol. % talc at the same heating rate of $20^{\circ}\text{C}/\text{min}$.

C. Shear rheometry of molten sample

Figure 8 shows the loss G' and storage G'' moduli determined at decreasing frequencies and various temperatures. Figures 8(a) and 8(b) clearly show that the rheological behavior has never reached the terminal region with the slope of 2 for G' and that of 1 for G'' . Instead, there are upturns at lower frequencies. The higher the temperature, the higher and earlier (i.e., lower frequency) the upturns are. The complex viscosity, $|\eta^*|$, shows the same behavior in Fig. 9(a). The LVE data show almost linear behavior and minimal shear thinning behavior at relatively high frequencies. However, $|\eta^*|$ shows an upturn with decreasing frequency rather than asymptotically approaches to the zero-shear viscosity. This behavior is similar to stereocomplex PLA,^{15,99} but the PLA used in this study has a very low D-content, so that stereocomplexity is not considered. The behavior is also similar to the case with microphase separation in polymers, such as block copolymer.⁷³ If there was a phase separation, it should have been between neat PLA and talc particles not among PLA polymeric chains. This type of behavior is similar to the typical viscosity (η) as a function of shear rate ($\dot{\gamma}$)¹⁰⁰ of steady simple shear for filled polymer systems. The viscosity curve can be divided into four sections, which can be observed in Fig. 10, where the first section is a plateau at very low shear rate, the second section is apparent yielding at low shear rate, the third section is an intermediate pseudoplateau, and the fourth section is

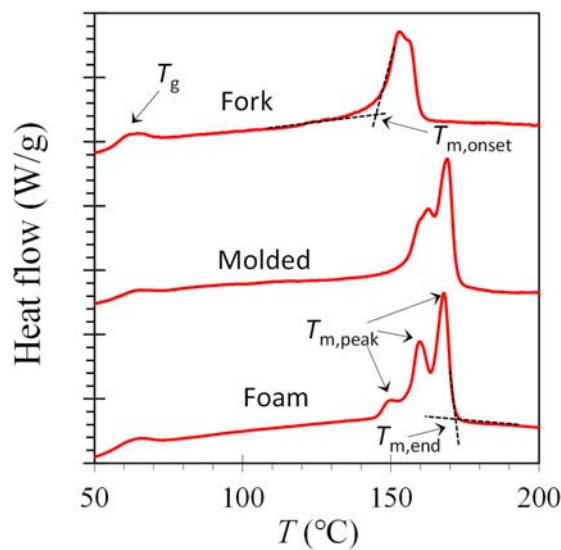


FIG. 7. Thermal behavior of three different samples during heating up at 20 °C/min. Each division on y axis is 0.1 W/g. Curves were shifted vertically to be all shown in the same plot.

shear thinning at high shear rate. There are two conflict contributions to the flow curve. Thus, two models can be added to model the whole viscosity curve vs shear rate¹⁰⁰ to cover nonhydrodynamic interaction, such as among particles and polymeric chains behavior at relatively low deformation rates, and hydrodynamic interaction among polymeric chains and behavior at relatively high deformation rates. Similar behavior can be expected in the frequency domain but due to the limitations of experiments, the first and last sections of the curve were not explored in this study. Thus, only the apparent yielding (an upturn with lowering frequency) and the pseudoplateau regions were observed and evaluated as shown in Fig. 9(a). The upturn should be due to the polar groups, i.e., hydroxyl groups and active sites on the talc surface.¹⁰¹ Talc particles tend to agglomerate, which result in the dynamic equilibrium between agglomeration and breaking up of the talc network during shear deformation.^{102–104} Shear deformation is often strong enough to break a capsule with thin membrane in liquid,¹⁰⁵ and thus loosely (physically) connected particles will be separated by shear deformation. The breaking up is dominant at high frequency (or shear rate) while agglomeration is dominant at low frequency leading to such an upturn. For these cases, shear history will be crucial since that arises the different network formations of talc. Considering that more talc network forms at low frequencies, the frequency sweep LVE measurements started from the highest frequency of 100 rad/s and moved to the lowest frequency.

The talc surface is both hydrophilic and hydrophobic at the same time,^{106,107} i.e., heterogeneous,¹⁰⁷ so hydrophilicity of talc should not simply induce the adhesion failure (or interfacial slip^{108,109}) between PLA and talc which is hydrophobic. Interfacial slip¹¹⁰ could also occur at high shear rates (or high stress) leading to a dramatic decrease on the complex and vice versa when the shear stress is relatively low. This could be confirmed by comparing the viscosity and the complex viscosity since the Cox–Merz rule³⁶ fails when interfacial slip takes

place¹¹¹ or by a visual method.¹¹² Considering that the instrument has limitations and interfacial slip is out of the scope of this study, the viscosity was not determined, and the visual method was not used. However, the trend shown in Fig. 10 should still be valid for the complex viscosity vs frequency since shear rate increases with frequency at a given strain. Since we have used a parallel-plate geometry, the deformation rate should depend on radial position unlike a cone-plate geometry.¹¹³ If cone-plate geometry was used, the results could be different. It should also be noted that the upturn could lead to large amplitude oscillatory shear (LAOS) flow^{114,115} and orientation of order in the flow.¹¹⁶ Since LAOS and the comparison between parallel-plate and cone-plate geometries are out of the scope of this study, this was not explored any further.

The apparent yielding at lower frequencies is a strong function of temperature as shown in Fig. 9(a). This could be due to the effect of temperature on hydrophilicity. Song *et al.*¹¹⁷ reviewed and studied the effect of temperature on the contact angle of water on a hydrophobic solid surface. They concluded the contact angle is invariant with temperature up to $T = 160$ °C even at various pressures. This implies that the interfacial tension between hydrophilic talc particles and hydrophobic PLA matrix can be a very weak function of temperature and that the change in interfacial tension with temperature does not account for the effect of temperature on the degree of the apparent yielding. As mentioned earlier, the apparent yielding is the result of the dynamic equilibrium of talc agglomeration and the mobility of polymeric chains. Thus, the viscosity of neat PLA is one of the key variables for the degree of the apparent yielding rather than interfacial tension. It is obvious that the viscosity of neat PLA matrix exponentially decreases with temperature. Thus, at a higher temperature, much lower stress (especially at lower frequencies) is imposed at a given deformation and deformation rate, i.e., driving forces to disturb network formation of talc is much lower. This results in poor dispersion of the talc particles and will eventually lead to the further increase in viscosity (more apparent yielding) of PLA/talc at a higher temperature and especially at lower frequencies. There are not enough data points since our results cover only the two regions. Hence, we have not tried to model using the combined two models, such as two Carreau–Yasuda models¹¹⁸ with different parameter sets as mentioned earlier. Figure 11 shows a sketch to illustrate how the frequency affects the network of talc particles. At either relatively low frequency, rate, or stress, the network of talc particles remains comparatively intact. This leads to dramatically higher complex viscosity than that of neat polymer while that is broken up at high frequency, so that talc particles are dispersed more evenly.

The strong effect of temperature on LVE, especially at low frequencies, implies that time-temperature superposition may not be successful throughout the whole curve of the LVE. However, we adopted a method used by Park *et al.*⁷³ We obtained the temperature shift factors by shifting the whole curves to make the sections only at high frequency, where hydrodynamic behavior is dominant, superposed. First, the vertical shift factors (density-temperature shift factors)³⁶ were obtained from the densities at various temperatures (Fig. 4) and is defined below,

$$b_T(T) \equiv \frac{T\rho_{0,\text{solid}}(T)}{T_{\text{ref}}\rho_{0,\text{solid}}(T_{\text{ref}})}, \quad (32)$$

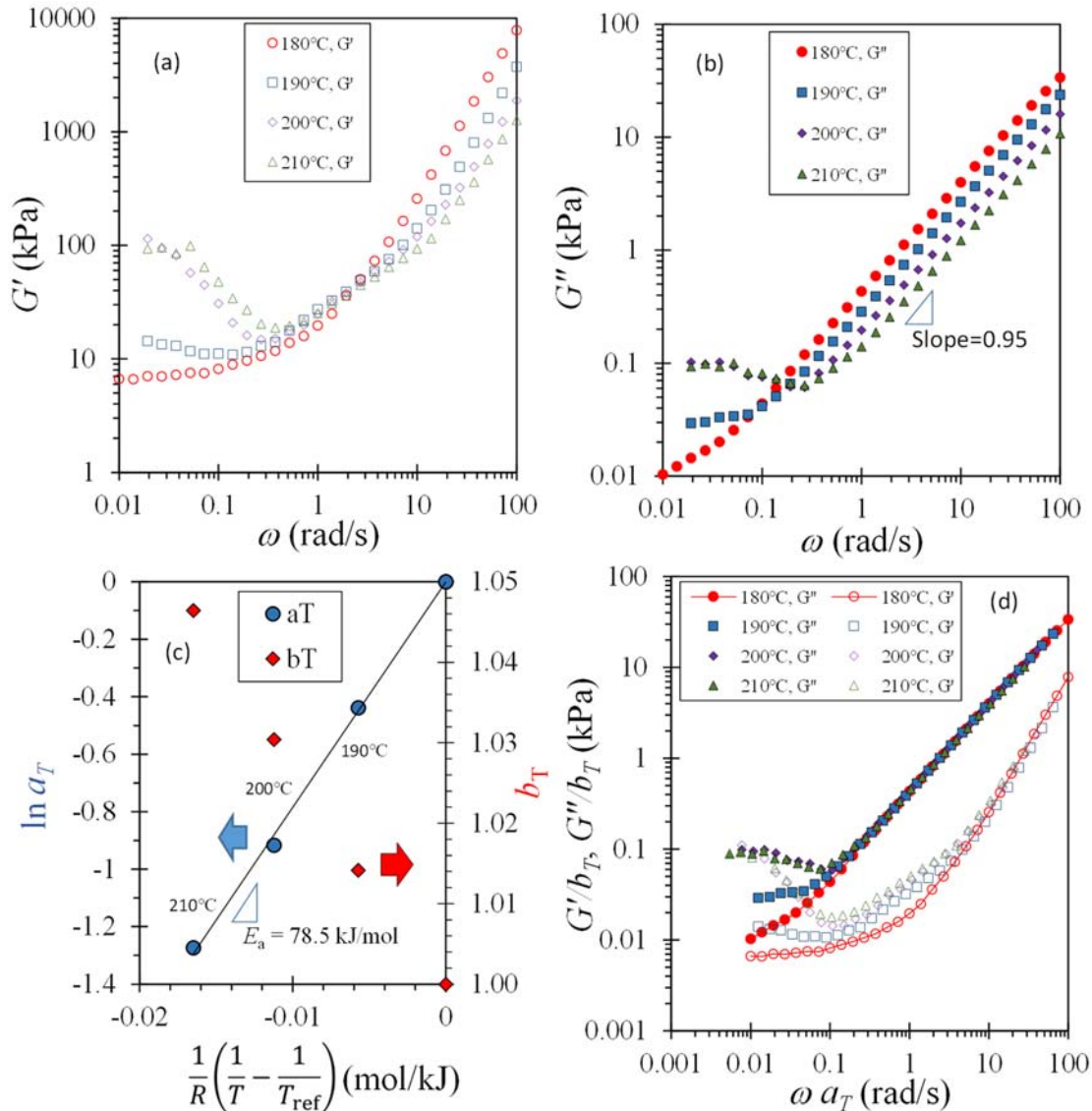


FIG. 8. Storage and loss moduli at various frequencies and temperatures. (a) Storage modulus, (b) loss modulus, (c) horizontal (time-temperature) shift factor and vertical (density-temperature) shift factor with Arrhenius model fit (solid line), and (d) reduced moduli using both density-temperature and time-temperature shift factors.

where temperatures are in K, and T_{ref} is the reference temperature of 180 °C, and applied to the moduli as $G'(T)/b_T(T)$ and $G''(T)/b_T(T)$. The vertical shift factor is often considered as unity, but this is not strictly true because that increases by 5% by 30 °C as illustrated in Fig. 8(c). Hence, these reduced variables were shifted to obtain the time-temperature shift factors, $a_T(T)$ as demonstrated in Fig. 8(c), until the high frequency sections are superposed on that at the reference temperature. Overall, the reduced variables can be plotted as shown in the above Fig. 8(d) and expressed with the following equations:

$$\frac{G'(T)}{b_T(T)} \quad \text{vs} \quad \omega(T)a_T(T), \quad (33)$$

$$\frac{G''(T)}{b_T(T)} \quad \text{vs} \quad \omega(T)a_T(T). \quad (34)$$

The time-temperature shift factor follows the classical Arrhenius equation¹¹⁹ and is expressed as

$$\ln a_T(T) = \frac{E_a}{R} \left(\frac{1}{T} - \frac{1}{T_{\text{ref}}} \right), \quad (35)$$

where E_a is the activation energy for the flow, and R is the ideal gas constant (8.314 J/mol K). The slope of Fig. 8(c) is $E_a = 78.5$ kJ/mol, and this value lies within the range of 71.9–80.9 kJ/mol¹⁷ for various

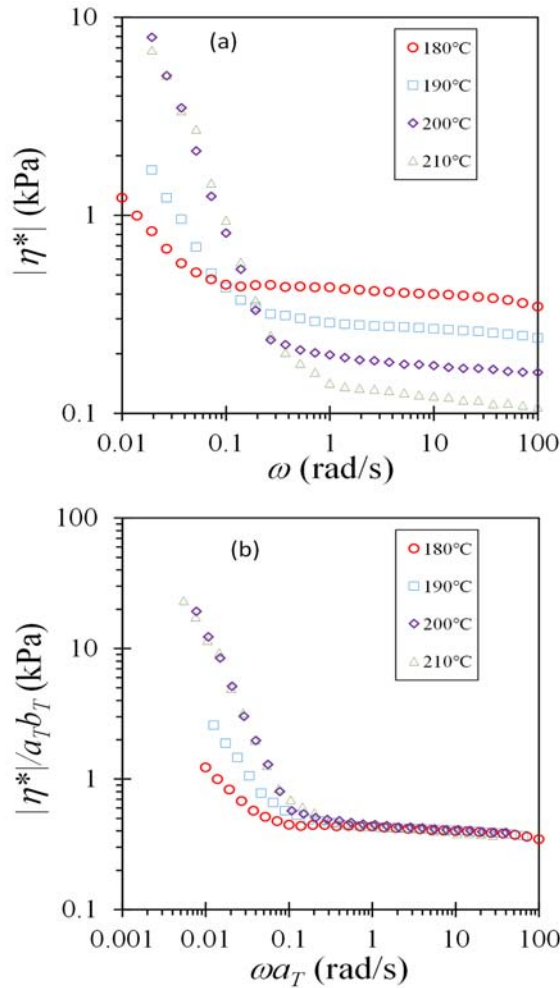


FIG. 9. Complex viscosity at various frequencies and temperatures. (a) Complex viscosity, and (b) reduced complex viscosity using both density-temperature and time-temperature shift factors.

PLAs, which had no talc and showed no apparent yielding. This implies that the behavior of PLA with or without talc is similar at high frequencies. Thus, the hydrodynamic behavior is clearly dominant at high frequencies, and the effect of talc is negligible.

The shift factors were applied to the complex viscosity as shown in the equation below,

$$\frac{|\eta^*|(T)}{a_T(T)b_T(T)} \text{ vs } \omega(T)a_T(T). \quad (36)$$

The above relationship can be seen in Fig. 8(b). As predicted, the complex viscosity at various temperatures can be superposed at relatively high frequencies, while low frequencies cannot be superposed due to the upturns. The onset frequency of upturn starts later with temperature, but the degree of upturn increases with temperature. The former implies that higher deformation rate, i.e., higher stress is necessary to break the network structure of talc particles at higher temperature due

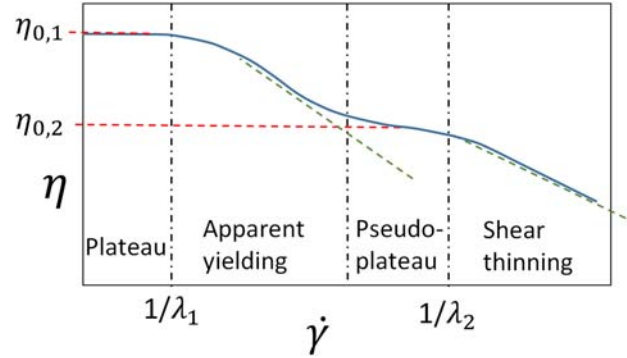


FIG. 10. Sketch of the log plot of viscosity vs shear rate for polymeric melt with filled solid.¹⁰⁰ The flow curve can be fitted to a combination of two models where η_0 is the zero-shear viscosity, and λ is the characteristic time in each model. The subscripts 1 and 2 indicate each model. Green dashed lines show power-law behavior.

to the low viscosity of the matrix. The latter implies that the network structure is stronger at higher temperature at the same deformation rate again due to the lower viscosity. However, the reduced complex viscosity at 200 and 210 °C is about the same implying that time-temperature superposition of the whole flow curve can be obtained at and above 200 °C. The rheological behavior above shows that the effect of compounded particular solid can be negligible in processes involving relatively high shear rate. On the other hand, it can be an issue in processes involving relatively low shear rate such in rotational molding and compression molding.¹²⁰ This is because small changes in thermal and/or shear history can lead to large changes in the behavior, since there is no strong shear stress to break the network structure of the particles resulting in low reproducibility. The particle size and its surface roughness also affect the flow matrix,¹²¹ and flow properties of one composite cannot be used for other composites with a different grade of talc. For continuous foaming process, additional variables, such as die swell will need to be considered.¹²² Since the effects of compounded various particles and die swell are out of the scope of this study, these were not further investigated.

D. Extensional rheometry of molten sample

1. Sagging issue

One of the major concerns in extensional rheometry is the sample sagging due to gravity and variations in strain rate. Sentmanat⁴⁶ minimized sagging issue by mounting a sample slab with an edge facing down in SER rather than having a large surface facing down. Thus, no supporting medium, e.g., oil¹²³ or gas¹²⁴ was necessary to support the sample when $\eta_0 > 10$ kPa s. We have not determined the viscosity but the following equality should be valid:

$$\lim_{\dot{\gamma} \rightarrow 0} \eta(\dot{\gamma}) = \lim_{\omega \rightarrow 0} |\eta^*(\omega)|. \quad (37)$$

Figure 9 shows $\lim_{\omega \rightarrow 0} |\eta^*(\omega)| < 1$ kPa s. Thus, η_0 of PLA/talc used in this study will be lower than 10 kPa s, and the sagging of the sample

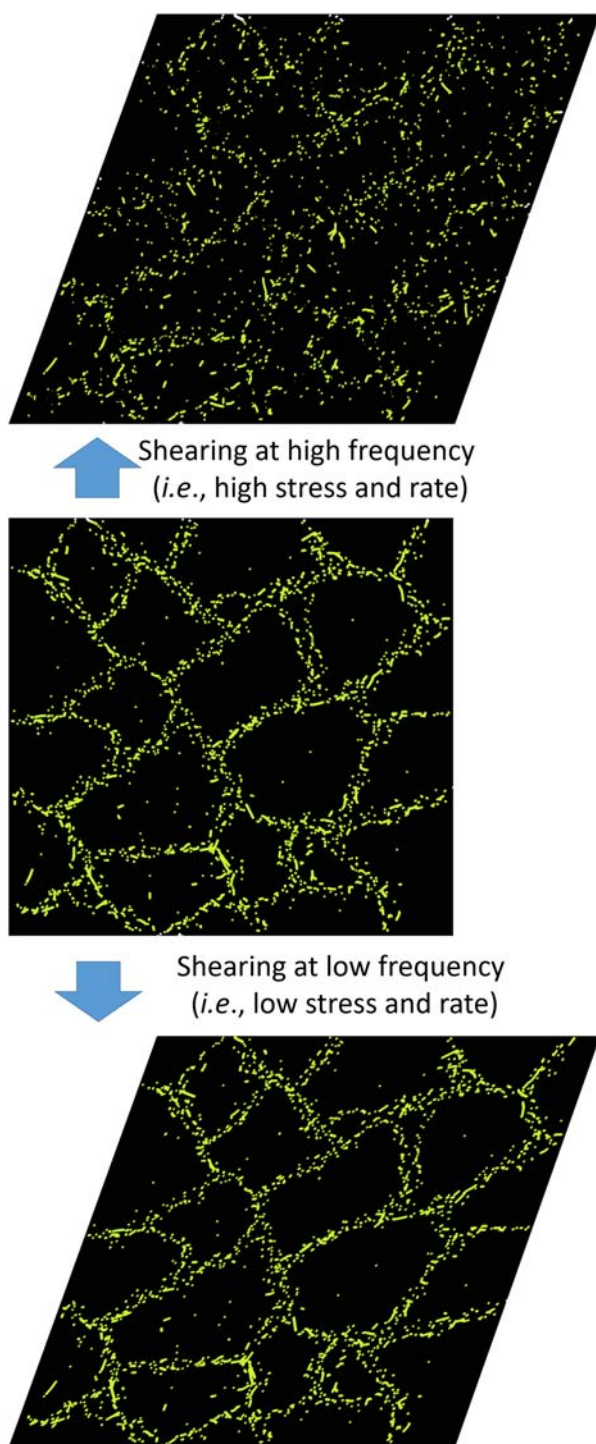


FIG. 11. Sketch of the network of talc particles (bright greenish yellow in polymer matrix (black), not based on model predictions. At either relatively low frequency, rate, or stress, the network of talc particles remains comparatively intact. This leads to dramatically higher complex viscosity than that of neat polymer while that is broken up at high frequency so that talc particles are dispersed more evenly.

in SER can be an issue. The sample will become thinner with the sagging or soaking time due to the downward stretching motion, and these make torque values during extension lower than those with no sagging present. Thus, if we use the same values in Eq. (9), we will underestimate $\eta^+(\dot{\epsilon}, t)$ due to the occurrence of sagging. Figure 12 shows the sagging behavior of a sample slab with 1 mm thickness at $T = 180^\circ\text{C}$. Sample sagging was shown even at soaking time, $t = 15$ s. While the upper edge became thinner first, the lower edge became thicker. After $t = 30$ s, the lower edge also starts sagging. To achieve fully molten state, it would be better to soak a sample at given temperature for as long as possible. Unfortunately, this approach is not valid and leads to serious sagging. Figure 13 shows $\eta^+(\dot{\epsilon}, t)$ at 1 s^{-1} after soaking the sample at $T = 180^\circ\text{C}$ for $t = 15, 30, 60$, and 120 s, respectively. The results clearly exhibit that $\eta^+(\dot{\epsilon}, t)$ decreases with soaking time, and this implies that the sample becomes thinner with elapsed soaking time. After $t = 120$ s, the lower edge almost touched the floor (shown in Fig. 12) and $\eta^+(\dot{\epsilon}, t)$ became erratic. Li *et al.*¹²⁵ developed a horizontal version of SER with a support underneath of the sample to avoid sagging. The working principle is similar to the Meissner type extensional rheometer,¹²⁴ but that development was not available for this study. The next question is how long we should leave the sample in SER before launching a test. We have chosen 30 s for this study. Extensional rheometry in this work has been performed to see if there is strain hardening. Even if the extensional rheometry underestimates the magnitude, it would not be a serious concern.

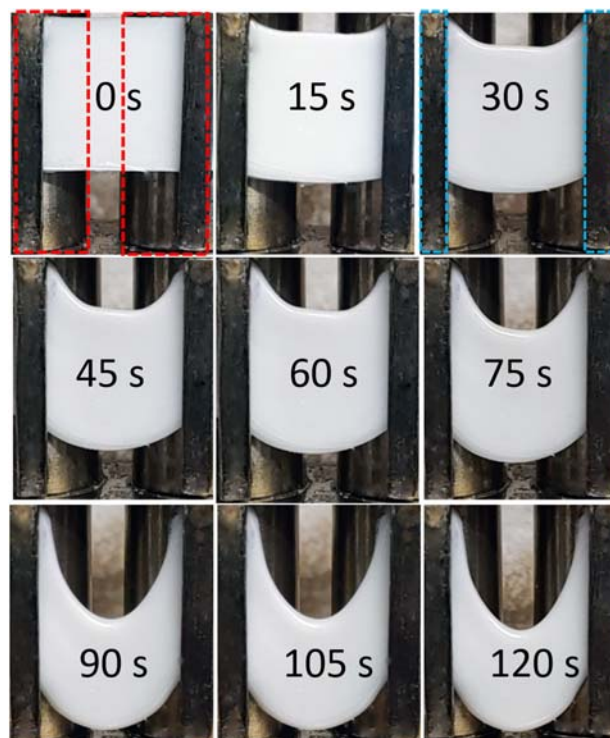


FIG. 12. Sagging behavior of 1 mm thick sample in SER with soaking time at $T = 180^\circ\text{C}$. Red boxes depict the location of the rotating drums while the blue boxes show where the sample clips are.

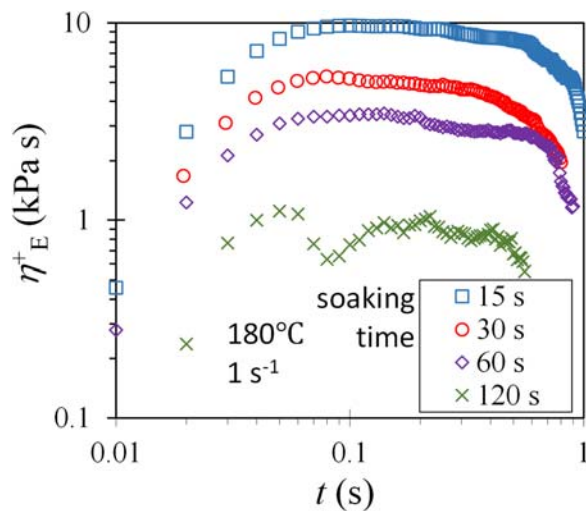


FIG. 13. Effect of sagging and soaking time on extensional properties at a Hencky strain rate of 1 s^{-1} and $T = 180^\circ\text{C}$.

One of the limitations of SER is extensional time especially at high strain rate. There is a sample holding clamp on each rotating drum. Both clamps are at the 12 o'clock position in the beginning and those can contact each other at 3 and 9 o'clock position after counter rotation if the sample is not thin enough. The contact leads to a surge in the torque and data beyond this point should not be used. If a sample is too thin, the signal to noise ratio may not be large enough, especially for the polymers with low viscosity. Thus, the sample should not be too thin to prevent that issue.

2. Effect of Hencky strain rate

Figure 14 shows the effect of Hencky strain rate ($\dot{\epsilon}$) on the tensile stress growth coefficient, $\eta^+(\dot{\epsilon}, t)$ after soaking the sample at $T = 180^\circ\text{C}$ for $t = 30 \text{ s}$. At various rates, $\eta^+(\dot{\epsilon}, t)$ shows nonlinear behavior, i.e., $\eta^+(\dot{\epsilon}, t)$ is dependent on $\dot{\epsilon}$. Due to the sagging issue, $\dot{\epsilon}$ lower than 0.75 s^{-1} was not used, so it is unknown if 0.75 s^{-1} shows linear behavior during longer periods of time. Dynamic shear deformations and extensional deformations will impose completely different stress profiles on the sample and this situation leads to different agglomeration of talc, especially at low deformation rates. Thus, the theoretical comparison between shear and extensional deformation may not be valid. In addition, we should not expect the three-times rule or the Trouton ratio to work: $3\eta_0 = \lim_{\dot{\epsilon} \rightarrow 0, t \rightarrow \infty} \eta^+(\dot{\epsilon}, t)$, where η_0 is the zero-shear viscosity and the viscosity in the pseudoplateau region (Figs. 9 and 10) in this study. Figure 13 shows $\lim_{\dot{\epsilon} \rightarrow 0, t \rightarrow \infty} \eta^+(\dot{\epsilon}, t) = 10 \text{ kPa s}$ for the case with minimum sagging while Fig. 9(a) shows that $|\eta^*| = 0.5 \text{ kPa s}$ in the pseudoplateau assuming that there is zero-shear viscosity in place, and the effect of talc network is negligible. This means $3\eta_0 \ll \lim_{\dot{\epsilon} \rightarrow 0, t \rightarrow \infty} \eta^+(\dot{\epsilon}, t)$, and hence it is difficult to discuss sagging with this comparison. This failure in applying the Trouton ratio seems to be due to the solid particles in the melt. It is easy to shear solid particles in a melt since those can be rotating¹²⁶ or translating. On the other hand, it is well more difficult to elongate

solid particles assuming there is no lip.¹²⁷ Such a theoretical comparison in detail is out of the scope of this work. However, it is quite obvious that there is no strain hardening behavior, which is often necessary for extending polymers.^{68,128} Since the PLA/talc used in this study does not show strain hardening, it could be difficult to foam. However, the setback can be overcome using optimized processing conditions of foaming, and identifying the operation window which were the aims of this study. Weingart *et al.*⁴³ recently showed that strain hardening is not the only key parameter to achieve low density foams. Linear polypropylene with no long chain branching structure (i.e., no straining hardening) could also be foamed to give a low foam density. Thus, it should not be discouraged to use polymers while they are not showing strain hardening behavior that is required for the foaming process. Weingart *et al.*⁴³ argued that slow crystallization can lead to a low foam density even without strain hardening. This was the motivation for us to choose low NPDR for foaming.

E. Tensile properties of solid samples

Figure 15 shows the tensile behavior of different samples with different thermal history, such as I: raw fork, II: compression-molded plate made from raw fork, III: twice compression-molded plate made from raw fork, and IV: compression-molded plate that was foamed and then compression-molded again. It is apparent that the raw fork (I) had the strongest tensile properties. This conveys that the compression-molding process weakens the samples and makes them less elastic. The toughness of the sample is a combination of tensile strength and elongation at break, as a result establishes the thermal history of toughness [Fig. 15(c)] to be more apparent than the results of tensile strength [Fig. 15(a)] or elongation at break [Fig. 15(b)].

Even so, it is surprising that the tensile properties for samples II through IV were relatively similar. This implies that once the first degradation due to compression-molding of the sample at $T = 190^\circ\text{C}$ exhausted the sample, further processing, such as foaming and another compression-molding, has less effect on the tensile properties, even

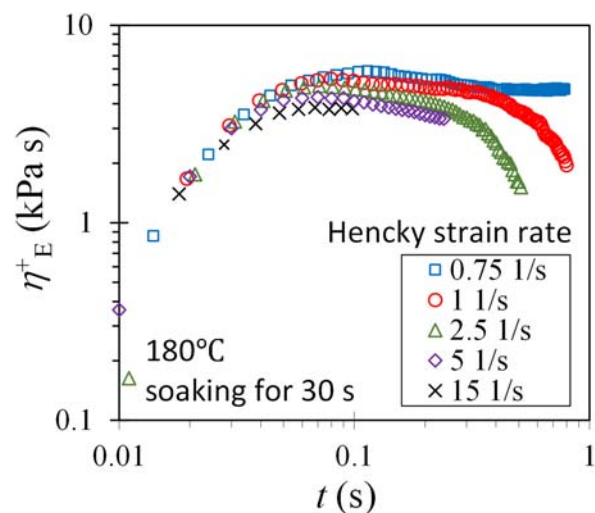


FIG. 14. Effect of Hencky strain rate on extensional property at $T = 180^\circ\text{C}$.

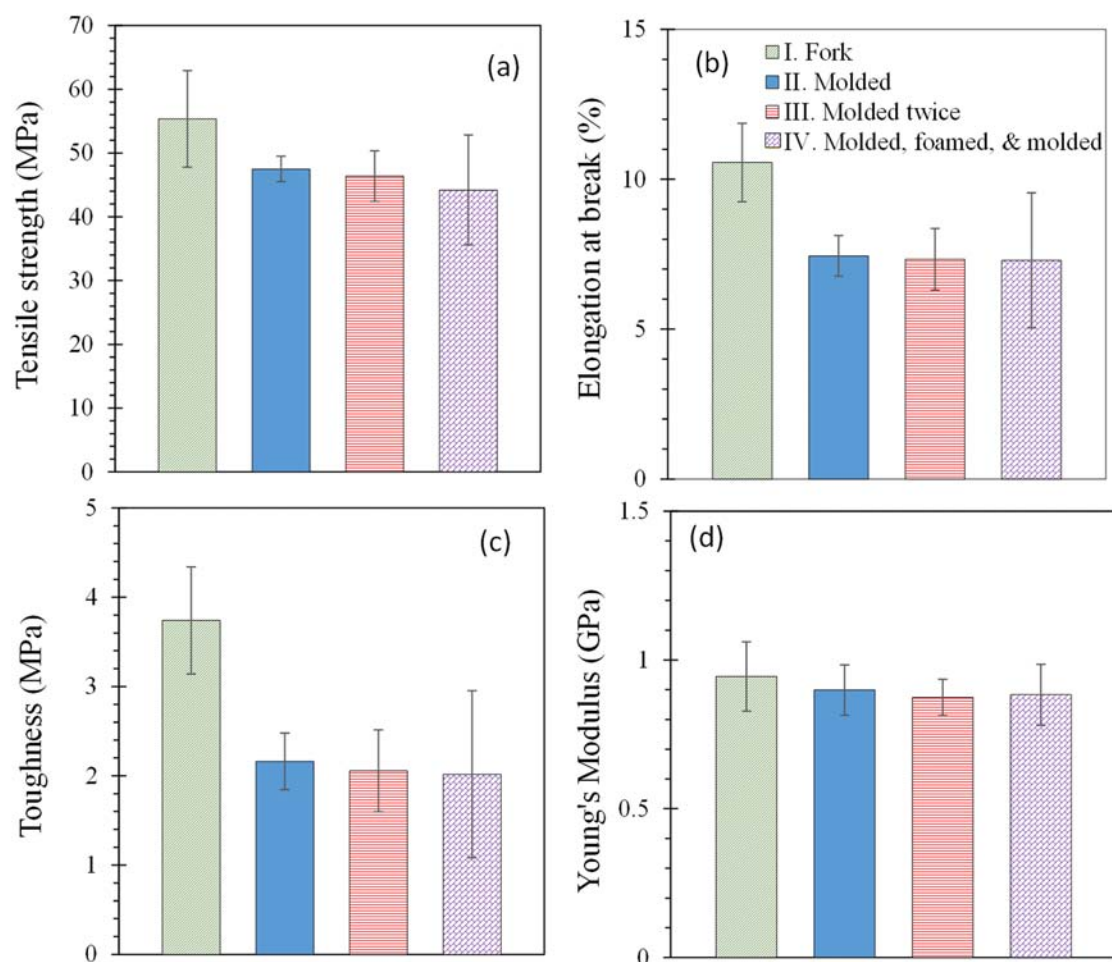


FIG. 15. Tensile properties of the four samples with different thermal history. I: Raw fork, II: compression-molded plate from raw fork chips, III: twice compression-molded plate, and IV: compression-molded plate that was subsequently foamed then cut into foam chips for re-molding. Error bars in the graphs show the standard deviations. (a) Tensile strength, (b) elongation at break, (c) toughness, and (d) Young's modulus.

though the standard deviation increases with thermal history. This situation is favorable since the recycling process can be repeated as the deterioration from further processing will be minimal. Compounded talc should have induced faster and more crystallization where it will lead to higher mechanical strength^{47,129} and thermal resistance. It should be noted that the thermal history of the raw fork and further processing of the samples had negligible effect on their Young's modulus [Fig. 15(d)]. This should be due to the fact that Young's modulus primarily expresses the rigidity of the samples rather than material strength. Overall, the rigidity of samples is not overly impacted by the further processing of the samples, which provides another incentive for recycling.

The PLA/talc composite used in this study showed no ductile behavior in tensile tests, and this disagrees to what Yu *et al.*⁴⁶ reported. Their PLA/talc composited with 0.3 wt. % of silane coupling agent (3-aminopropyltriethoxysilane, KH-550) and up to 30 wt. % of talc showed an increasing trend in ductility as well as in their tensile

strength, toughness, and elongation at break. Especially elongation at break, it was tripled when 30 wt. % of talc was added. These escalated properties were predominantly due to the coupling agent which reduced the material's adhesive failure. However, the tensile strength of the material composite only increased by 10% even though the crystallinity increased by eight times while adding 30 wt. % of talc. This implies that the tensile strength is a weak function of crystallinity while the elongation at break is a strong function of that, but this is the case with the coupling agent.

F. Properties of foams

1. 1D vs 3D and effect of NPDR

To study the effect of expansion direction on foam properties, we performed foaming in 1D (expansion only vertically) and 3D (expansion not only vertically but also radially) at $T = 180^\circ\text{C}$, $P = 10\text{ MPa}$, and NPDR [Eq. (11)] of 0.06, 0.13, and 0.16 s^{-1} . The conventional

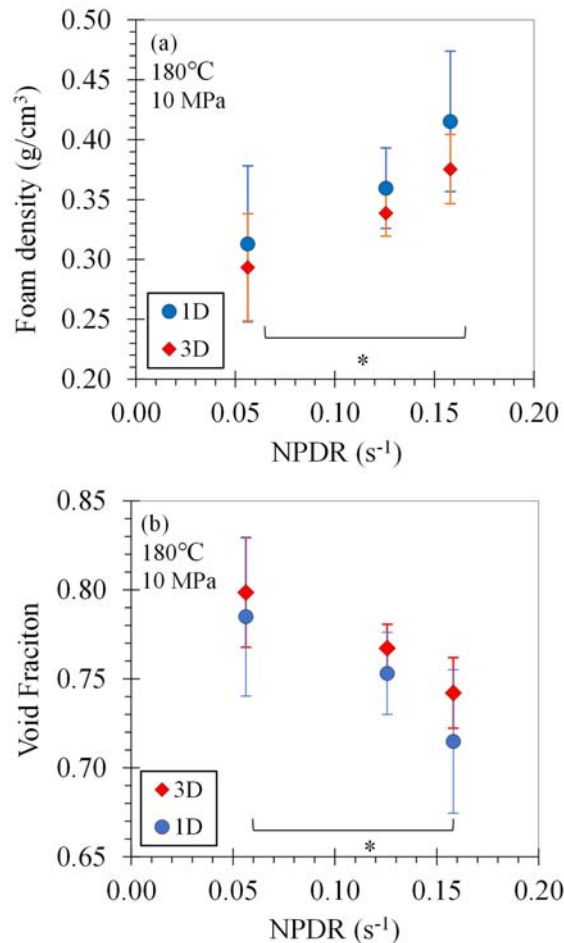


FIG. 16. Comparison of (a) foam density and (b) void fraction [Eq. (28)] for 1D and 3D foams at NPDR = 0.06, 0.13, and 0.16 s⁻¹. The conventional pressure drop rates (PDR) for these are 0.8, 1.5, and 2.3 MPa/s, respectively. Error bars represent the standard deviation. *: $p < 0.05$.

pressure drop rates, PDR [Eq. (10)] right after opening the valve for those NPDRs were 0.8, 1.5, and 2.3 MPa/s, respectively. The 3D foaming was indeed 2D expansion, i.e., in the radial and longitudinal in cylindrical coordinate system. From our preliminary studies, we found that irregular cell structures rupture at relatively high NPDR. Such ruptures can be due to the large strain during expansion after fast crystallization even if the matrix was still soft.¹³⁰ In regard to this manner, we have chosen relatively low NPDR values for the comparison of 1D [Fig. 3(b)] and 3D [Fig. 3(a)] foaming. The foam density, $\rho_{0,\text{foam}}$ [Eq. (19)], and the void fraction, f_{cell} [Eq. (28)], were determined by taking the average over four replicates as shown in Fig. 16. Through analysis, we observed that 1D foaming results in denser foams. It is manifest that the restriction in radial direction suppressed the overall foam expansion. Foam expansion was concentrated in longitudinal direction, which means there should be more expansion in that direction than in 3D, yet it was not the case. There should have been expansion in radial direction as well in 1D foaming, and this phenomenon can be seen based on

Fig. 17, which illustrates the side view of cell structures after cutting samples vertically, i.e., orthogonal to the bottom surface [Fig. 5(a)]. As for Fig. 18, it shows the top view of cell structures after cutting samples horizontally, i.e., parallel to the bottom surface [Fig. 15(b)]. In 1D foaming, voids were formed in the radial direction which denotes expansion in that direction. However, the diameter of the constraining cylinder was the same as the disk diameter, which means the disk should not be able to expand in the radial direction. In regard to this occurrence, the voids were replacing the polymer matrix by pushing the matrix upward in the longitudinal direction while expanding in radial direction. This is similar to air bubble propagation in a rectangular elasto-rigid channel¹³¹ where the matrix has a fixed width, but an air bubble grows. It should be noted that there was no significant statistical difference between 1D and 3D foams as illustrated in Fig. 17. This suggests that in either 1D or 3D foams, there was only minimal expansion in the radial direction. Moreover, the samples were thin disks, which implies that it would be easier to expand in longitudinal direction rather than radial direction and can be observed in Figs. 17 and 18.

Both the foam density and void fraction are dependent on the NPDR for both 1D and 3D expansions. The foam density increases and the void fraction decreases with NPDR, indicating that foaming should take place in a slower manner (i.e., at low NPDR) to make bulky foams at the given conditions. The higher the NPDR, the faster

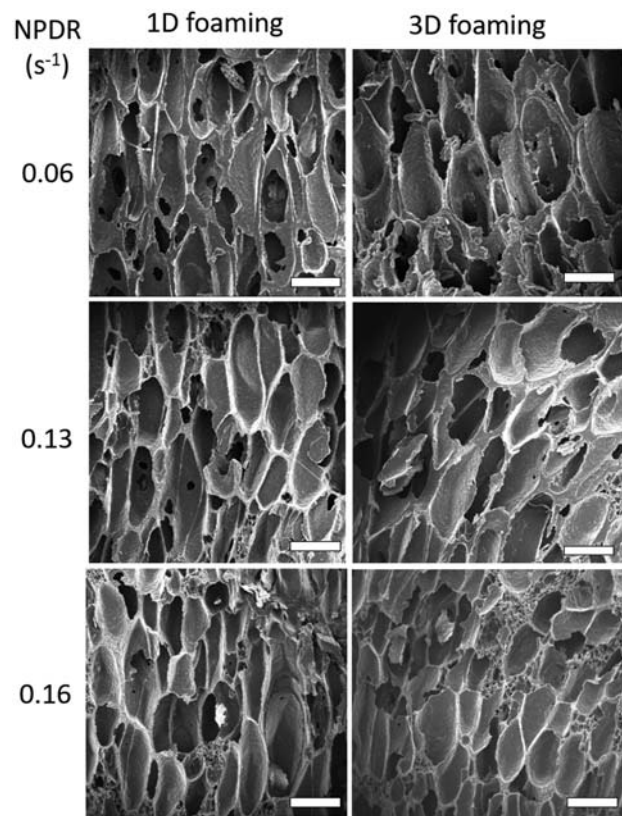


FIG. 17. Side view of the cell structure after cutting the samples in a direction that is orthogonal to the bottom surface [Fig. 17(a)]. White scale bars are 500 μm long.

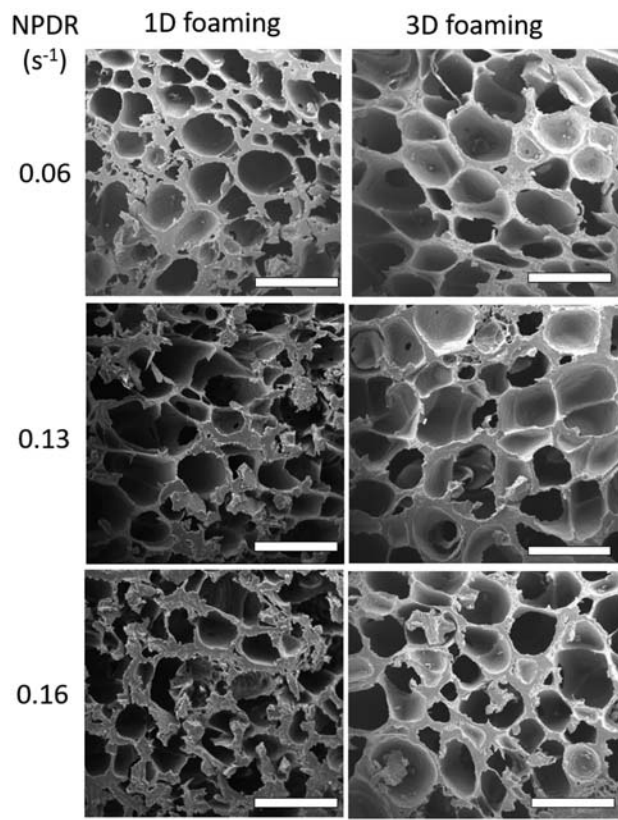


FIG. 18. Comparison of the top view of the cell structure after cutting the samples in the direction that is parallel to the bottom surface [Fig. 17(b)] for 1D and 3D foams at NPDR = 0.06, 0.13, and 0.16 s⁻¹. The conventional pressure drop rates (PDR) for these are 0.8, 1.5, and 2.3 MPa/s, respectively. White scale bars are 500 μ m long.

the sample temperature drops. This leads to faster solidification and stabilization of the cell structures rather than allowing the cells to grow slowly. The temperature depression due to pressure drop would increase with NPDR. Thus, foaming at high NPDR leads to the glass transition temperature being more quickly attained, and quicker solidification inhibits cell expansion. For those reasons, smaller cell structures and denser foams will be obtained. These trends are correlated with the theories^{79,80,132} regarding cell nucleation and growth. The effect of NPDR will be discussed along with the cell density subsequently.

Figure 19(a) shows the comparison of the cell diameter in 1D and 3D foams, and those values were obtained from the top view of the cells (Fig. 18). The standard deviation of the values appears to be rather substantial because there is a large size distribution. In addition, the cells are not simply cylindrical and the size of the cells in the SEM images varies with the location of the foam cutting. The cell diameter of 1D foaming is slightly smaller than that of 3D foaming even though there is a significant statistical difference. This contingency should be due to the constraint in the radial direction in 1D foaming. We should also analyze the cell circularity [Eq. (22)] obtained from side view of cells as illustrated in Fig. 19(b) to consider the effects of

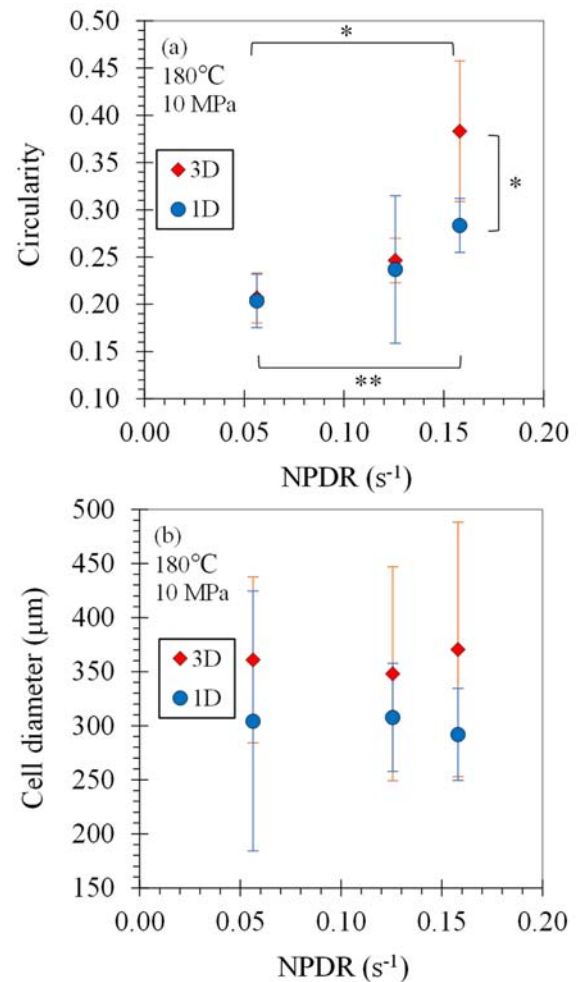


FIG. 19. Comparison of (a) cell diameter obtained from the top view of cells and (b) cell circularity obtained from side view of cells for 1D and 3D foams at NPDR = 0.06, 0.13, and 0.16 s⁻¹. The conventional pressure drop rates (PDR) for these are 0.8, 1.5, and 2.3 MPa/s, respectively. Error bars represent the standard deviation. *: $p < 0.05$ and **: $p < 0.01$.

NPDR and foaming direction on cell structures. Although there is no significant difference in 1D and 3D cell circularity, generally the circularity of 3D foams will be larger than 1D foams. Nevertheless, this does not convey that cells in 3D foams were less elongated vertically than 1D because the cell diameter of 3D foams is larger. Furthermore, the circularity of both 1D and 3D foams increases with NPDR, but the cell diameter is invariant with NPDR [Fig. 19(a)]. A faster pressure drop induces faster solidification, as a result in less cell growth longitudinally, i.e., less expansion resulting higher foam density which is illustrated in Fig. 16. However, there is minimal effect of NPDR on horizontal (radial) cell growth, which was expected. This is because it will require more time for the cells to complete vertical growth than radial growth considering that the aspect ratio, and radial growth was well completed before vertical growth and stopped by solidification, i.e., cooling process.

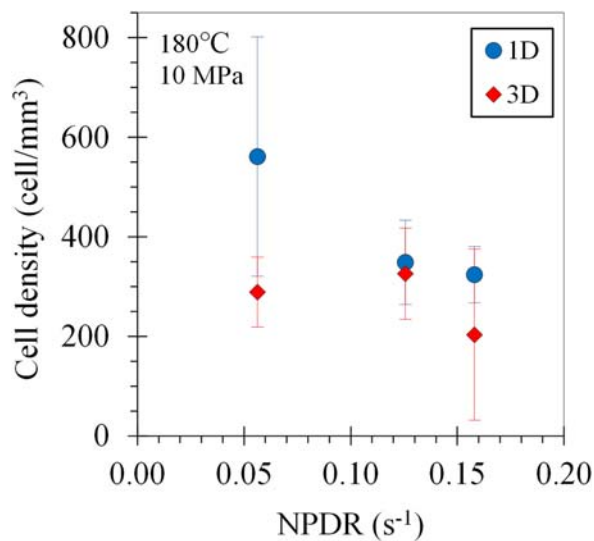


FIG. 20. Comparison of the cell density for 1D and 3D foams at NPDR = 0.06, 0.13, and 0.16 s⁻¹. The conventional pressure drop rates (PDR) for these are 0.8, 1.5, and 2.3 MPa/s, respectively. Error bars represent the standard deviation.

Figure 20 shows the comparison of the cell density, ρ_{cell} [Eq. (21)]. Cell density described in Eq. (21) still significantly lacked accuracy since the cell density was estimated only from a 3D micrograph. To improve the accuracy of cell density, a “correction factor, which is governed by the foam structure and cell growth direction, was factored in Ref. 133. However, it was not possible to obtain the exact correction factor since the cell shape varies. Figure 20 shows that there is no particular statistical difference between 1D and 3D foams, but we can observe an established relationship. In comparison with 3D and 1D foams, cell density of 3D foams is lower than 1D foams at given NPDR. This relationship denotes that the thermodynamic instability due to sudden pressure drop in the 1D foaming process was more utilized for nucleation rather than cell growth, due to its constraints, i.e., can only expand in one direction in contrast with the 3D foaming process, i.e., can expand in two directions. In other words, the cell density decreases with NPDR, and this trend contradicts others' work.^{79,80,132} They reported that the cell density of foams increases while cell diameter decreases with PDR due to its high thermodynamic instability. Even so, their PDR was considerably larger than ours, and the cell density may show a U-shaped trend with NPDR.

The talc particles have served as a nucleating agent for both crystallization and foaming, i.e., heterogeneous nucleation¹³⁴ that leads to faster solidification (less cell growth) and higher cell density^{135,136} than foaming neat polymers. The average cell size in Fig. 19 shows that the foams made at the given conditions ($T = 180^\circ\text{C}$ and $P = 10\text{ MPa}$) can be classified as conventional and fine-celled foams.⁴⁰ The distribution of cell size is rather large, and that is even larger in 3D foaming. This fact should not discourage us recycling PLA to make foams. Foams made from recycled PLA cutlery can still be used in applications which do not need uniform cell size. On the basis of pycnometer measurements, the closed cell fraction [expressed in Eq. (30)] was determined to be zero at all foaming conditions. This suggests that all cells were

open, i.e., only open-cell foams¹³⁷ were produced in this study. The remaining CO₂ in the foams should have been replaced by air quickly unlike closed-cell foams, which require more time due to lower diffusivity.¹³⁸ Nofar *et al.*¹³⁹ explained that reduced melt strength increases the open cell fraction in PLA foams. As mentioned earlier, the melt strength and even the tensile strength of PLA in this study were obtained to be relatively low. Therefore, we should expect that we will obtain low cell wall strength during the foaming process. McInerney *et al.*¹⁴⁰ showed that the elasticity of polypropylene decreases with the talc content between 5 and 25 wt. %. In addition, Kaewmesri *et al.*¹⁴¹ argued that too much talc compounded in PLA can increase the open cell fraction. It is due to the talc particles in PLA that serves the breakage of the polymeric matrix during cell expansion. Overall, we can consider applications of recycled PLA/talc in the fields requiring open cells, such as sound insulators,^{142,143} oil production,¹⁴⁴ filters,¹⁴⁵ and wicks for evaporative humidifiers. It is favorable to have various pore structures since we can expect different drying behaviors of liquid

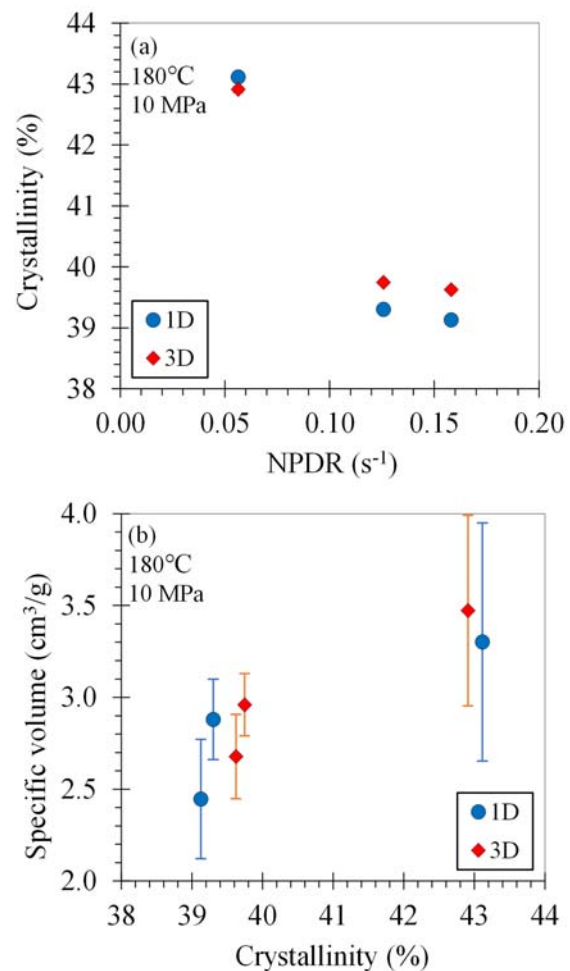


FIG. 21. (a) Effect of NPDR on crystallinity of foams and (b) effect of crystallinity on specific volume.

from the pores for different humidifiers considering that various pore structures among different foams lead to different Kelvin effects.¹⁴⁶

Crystallinity and the crystallization kinetics are the two key variables that affect the foam structure significantly. Figure 21 illustrates that the crystallinity of foams is strongly dependent on NPDR even though there is no significant difference between 1D and 3D foams. It clearly demonstrates that the crystallinity decreases with NPDR since polymer chains would have less time to crystallize due to the rapid temperature drop at a higher NPDR. From a glance, foam density would increase with crystallinity since higher crystallinity indicates higher rigidity thus increased difficulty in cell expansion. Nevertheless, Fig. 21 suggests that the specific volume of the foams increases as crystallinity increases. This is because prior flow history significantly affects crystallization.¹⁴⁷ For example, during the pressure drop of the foaming system, shear-induced crystallization and extension-induced crystallization can occur. As a result, the more the polymer expands, i.e., resulting higher specific volume, the higher the crystallinity.

2. Effects of temperature and pressure

It is important to understand the effects of the processing variables on the foam properties because those are the control variables to produce proper foams for specific applications. However, whether it is batch or continuous physical foaming, it will be a very complicated process that involves many different variables and phenomenon. This is because not only the process conditions but also the bubbles will significantly affect the flow properties of the matrix¹⁴⁸ and bubble growth. Moreover, the adjacent bubbles will affect the behavior of each other,¹⁴⁹ such that bubbles can also interact with solid particles,^{150–153} bottom floor,¹⁵⁴ and a free surface.¹⁵⁵ In addition, the solidification of matrix also affects the expansion of the matrix.¹⁵⁶ If a composite with ceramic particles was used as in this study, the gas–solid interaction,¹⁵⁷ movement of the particles,¹⁵⁸ relation between transport phenomena and thermodynamics,¹⁵⁹ and the assembly of the particles due to the generation of strong acoustic noise¹⁶⁰ during foaming will be the additional variables to the process. Thus, it is not possible to separate an effect of one variable from other variables in relation to foam properties, but we can still analyze the certain effects of variables. We performed 3D foaming [Fig. 3(a)] at pressures (P) of 10, 20, and 28 MPa, at temperatures (T) of 140, 160, and 180 °C, and at one NPDR. Based on the study shown in Sec. III F 1, bulkier foams can be made at low NPDR. Hence, we have chosen 0.02 s^{-1} as the NPDR [Eq. (11)] to study the effects of temperature and pressure. The initial conventional PDR [Eq. (10)] is 0.2 MPa/s at 10 MPa, 0.4 MPa/s at 20 MPa, and 0.6 MPa/s at 28 MPa for NPDR = 0.02 s^{-1} .

Figure 22 shows the effects of temperature and pressure on the foam density. In general, the foam density decreases with temperature and increases with pressure. Likewise, it should be more difficult to expand at low temperature and high pressure due to the high viscosity of the polymer matrix and rapid temperature dropping below the crystallization temperature. Even though NPDR [Eq. (11)] with the units of s^{-1} is better representative for the whole depressurization process, PDR [Eq. (10)] with the units of MPa/s can be another variable. The higher the pressure is, the higher PDR at given NPDR. Thus, depressurization is stiffer with time at a higher pressure even though it takes the same time to complete depressurization at the same NPDR. This conveys that the temperature decrease is faster, i.e., faster solidification at a higher pressure than at a lower pressure at the same NPDR.

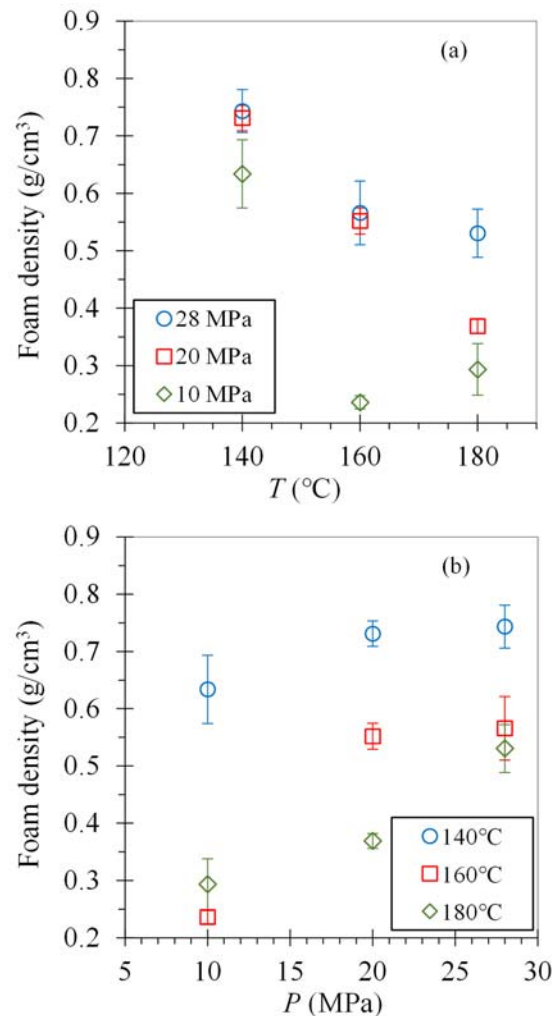


FIG. 22. Effect of sorption temperature and pressure on the foam density. NPDR = 0.02 s^{-1} . Error bars represent the standard deviation. (a) Effect of temperature on foam density at various pressures and (b) effect of pressure on foam density at various temperatures.

However, there is one exception at 10 MPa, at which the density shows a V-shaped behavior [Fig. 22(a)]. At the lowest pressure of 10 MPa, temperature drop rate is the lowest and the viscosity should also be the lowest. Meanwhile, $T = 140^\circ\text{C}$ is too low for large cell expansion and 180°C is too high to give a high concentration of CO_2 , i.e., there is less CO_2 in polymer than 160°C .

Figure 23 shows the top view of the cell structures after cutting the samples parallel to the bottom surface [Fig. 5(b)]. It is observed in Fig. 23 that significantly different foam structures can be obtained by varying sorption temperature and pressure at the same NPDR. This is due to the fact that the effects of sorption temperature and pressure are significant.

Figure 24 shows the effects of temperature and pressure on the cell diameter. Generally, the cell diameter increases with temperature and decreases with pressure. This means it is expected that the

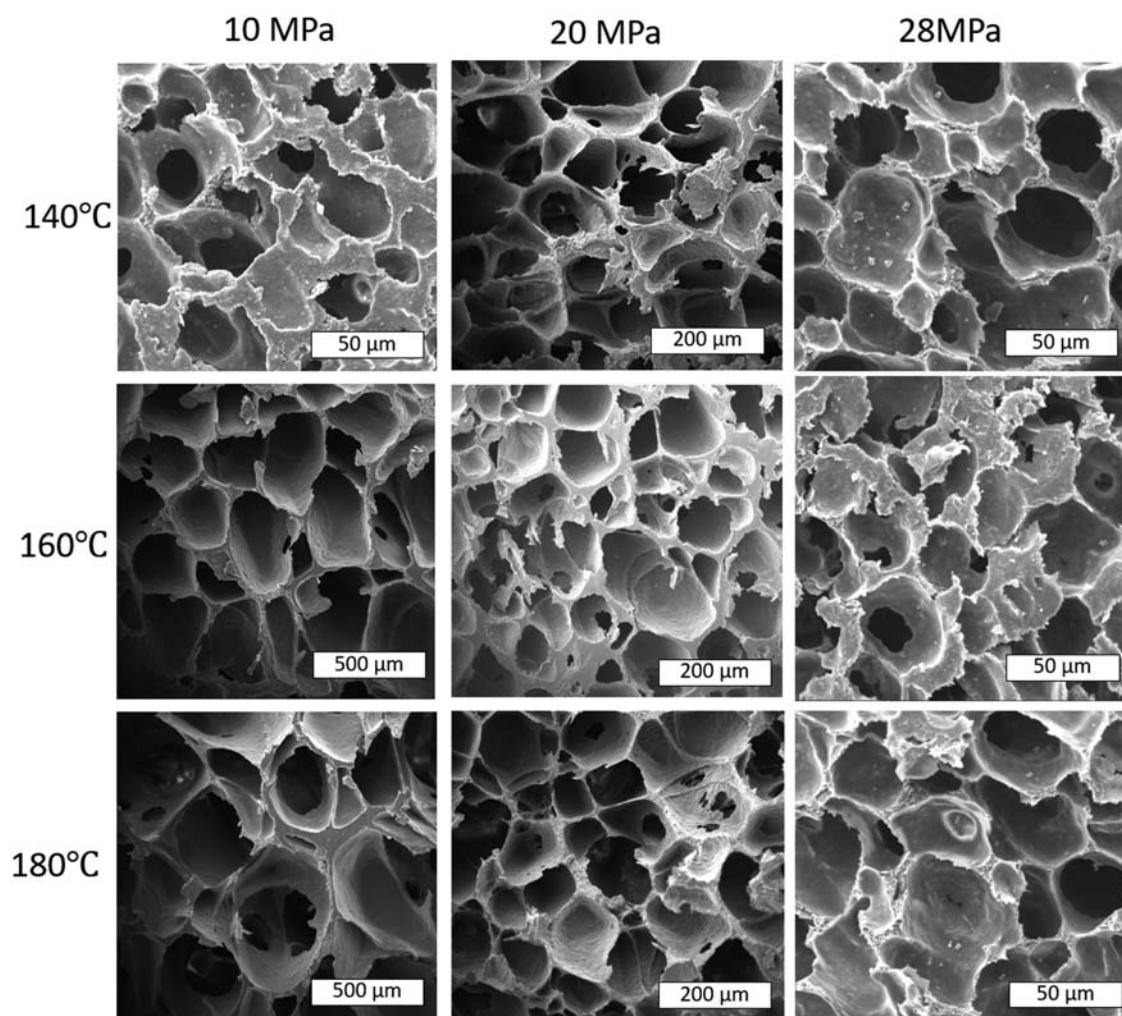


FIG. 23. Comparison of the top view of the cell structure after cutting samples in the direction that is parallel to the bottom surface [Fig. 17(b)] at various temperatures and pressures at NPDR = 0.02 s⁻¹.

polymer can expand more at a higher temperature and lower pressure due to the lower viscosity. In spite of that, the CO₂ concentration will be lower at higher temperature and lower pressure. Thus, even at high CO₂ concentration, we cannot expect more cell expansion. The cell diameter decreases with pressure at $T = 140^\circ\text{C}$. This suggests that the viscosity increases at high pressure and suppresses cell expansion. The cell diameter at $T = 140^\circ\text{C}$ and $P = 10\text{ MPa}$ in Fig. 24(b) does not appear to follow the expected trend. Park and Dealy⁵⁶ reported that the viscosity of polymer/CO₂ decreases with the pressure (and thus CO₂ concentration) due to the significant plasticization even though pressure exponentially increases the viscosity. The state of PLA/talc sample at such a low temperature of $T = 140^\circ\text{C}$ might be solid especially at low pressure due to low plasticization. In this manner, cell expansion may have been suppressed. The average cell size in Fig. 24 shows that the foams made at the given conditions can be classified as fine-celled foams.⁴⁰

Figure 25 shows the effects of CO₂ sorption temperature and pressure on the cell density. The cell density decreased with temperature, which is the opposite trend to cell diameter except at $P = 28\text{ MPa}$. The cell density either increases with pressure (at $T = 180^\circ\text{C}$) and shows a V-shaped relationship with pressure (at $T = 140$ and 160°C). As mentioned earlier, PDR increases with pressure at a given NPDR. The sudden pressure drop gives rise to thermodynamic instability which causes less time for CO₂ to expand cells. As a result, it induces more nucleation occurrence at $P = 20\text{ MPa}$ and above. On the other hand, at relatively low temperatures, i.e., $T = 140$ and 160°C , it is difficult for cells to expand due to the higher viscosity at a lower CO₂ pressure (or concentration). Hence, more nucleation occurs rather than cell growth.

Figure 26(a) shows the effect of pressure and temperature on the crystallinity of foams. The results do not seem to portray a clear trend unlike the effect of NPDR [Fig. 21(a)]. As for Fig. 26(b), it describes

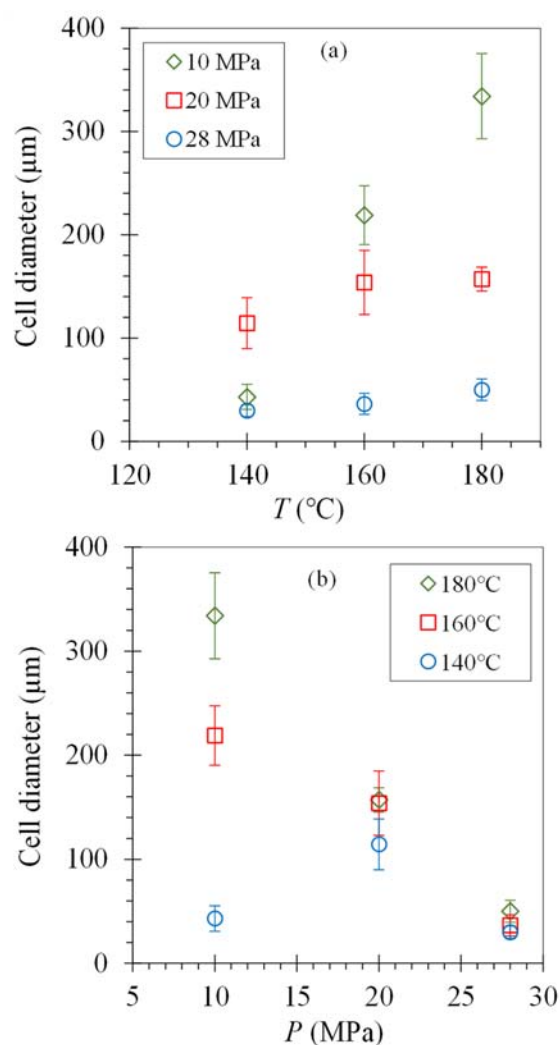


FIG. 24. The effects of sorption temperature and pressure on the cell diameter. NPDR = 0.02 s^{-1} . Error bars represent the standard deviation. (a) Effect of temperature on cell diameter at various pressures and (b) effect of pressure on cell diameter at various temperatures.

the effect of crystallinity on the specific volume of the foams. Similarly in Fig. 26(a), there does not seem to be an apparent trend in the results except for $T = 180^\circ\text{C}$. The results reflect that the bulkiness of foams roughly decreases with crystallinity. From the analysis, specific volume increases with crystallinity above 29% [Fig. 21(b)], and the relation between the specific volume and crystallinity seems to be V-shaped (Fig. 29). These trends will be briefly discussed in the last section.

3. Key variables affecting specific volume

As mentioned earlier, several variables are involved in physical foaming which makes it difficult to use one variable to predict the foam properties. However, Fig. 27 illustrates that the specific volume

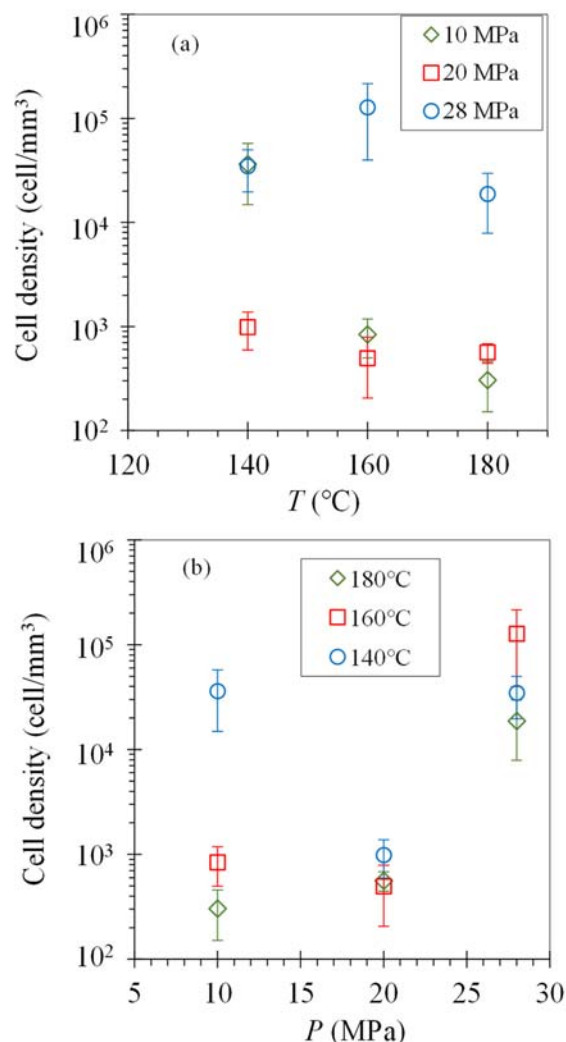


FIG. 25. The effects of sorption temperature and pressure on the cell density. NPDR = 0.02 s^{-1} . Error bars represent the standard deviation. (a) Effect of temperature on cell density at various pressures and (b) effect of pressure on cell density at various temperatures.

decreases as the concentration of CO_2 increases in spite of the sorption temperature and pressure at given NPDR of 0.02 s^{-1} . It was expected that dissolving more CO_2 will result bulkier foams, but the trend was the total opposite. It is not just the high CO_2 concentration that directly induces denser foams, but rather than the combination of low temperature and high pressure that provides high CO_2 concentration that give rises to denser foams. The interfacial tension as a function of pressure and temperature¹⁶¹ should also affect the cell growth and stability. Additionally, the crystallinity should contribute to the foam structures but it is not a strongly representative variable for prediction as shown in Fig. 26(a). As observed in Fig. 22, the foam density was high at low sorption temperature and at high sorption pressure. Overall, the effects of the foaming temperature and pressure were more predominant than the concentration of CO_2 in the polymer.

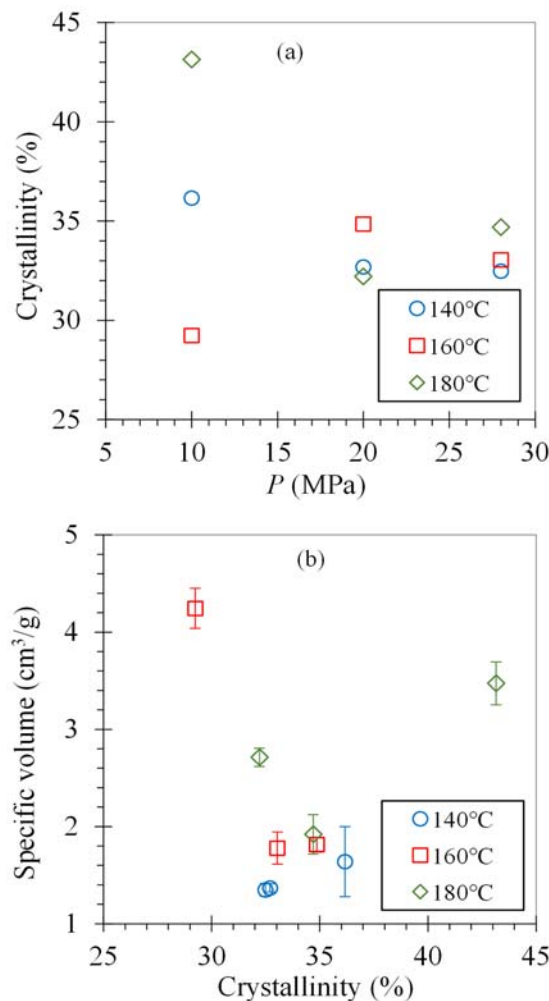


FIG. 26. The effects of sorption temperature and pressure on the crystallinity of foams and the effect of crystallinity of the specific volume of the foams. NPDR = 0.02 s^{-1} . Error bars represent the standard deviation. (a) Effect of pressure on crystallinity at various temperatures and (b) effect of crystallinity on specific volume at various temperatures.

Nevertheless, CO_2 concentration could be a single, representative and an independent variable to describe the behavior of the specific volume as a whole. However, in Fig. 28, there is no apparent relation between the cell density and CO_2 concentration.

Crystallinity of foams can be another key variable that influences the specific volume of foams. In Fig. 29, a V-shaped trend between crystallinity and specific volume is observed. Crystallinity has two opposing effects on cell expansion. First, it can provide strength during the foaming process so that it can reduce the chances of cell collapsing or coalescence.^{67,162} On the other hand, it can suppress elasticity. The latter effect is dominant up to a crystallinity of 27% while the former effect is dominant above 27%. It should be noted that the crystallinity can only be after foaming, and the specific volume cannot thus be predicted before implementing the foaming process.

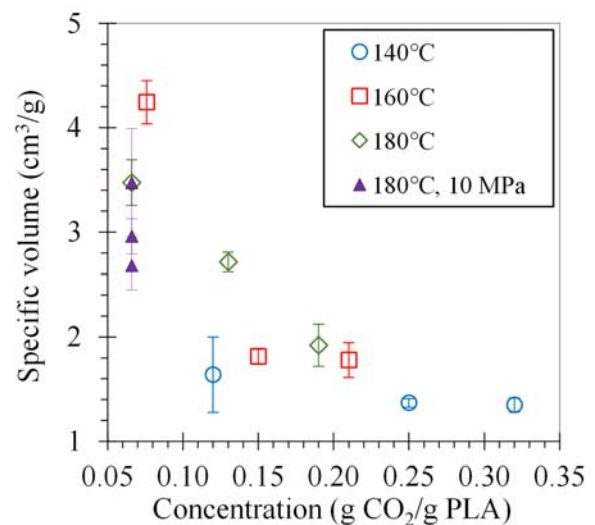


FIG. 27. Effect of CO_2 concentration on specific volume. Closed symbols are for data obtained at 180°C and 10 MPa and at various NPDR (3D), and open symbols are for data obtained at NPDR of 0.02 s^{-1} and at various P and T . Error bars represent the standard deviation.

IV. CONCLUSIONS

We hypothesized that PLA cutlery, which was not made of a foaming grade, can be physically foamed using supercritical carbon dioxide (CO_2). This required optimizing the operating variables, such as, CO_2 sorption temperature, sorption pressure, and pressure drop rate to be able to produce foams from the PLA cutlery. This approach is crucial to attain the details regarding the possibility of recycling biodegradable plastics, which were not initially designed for recycling.

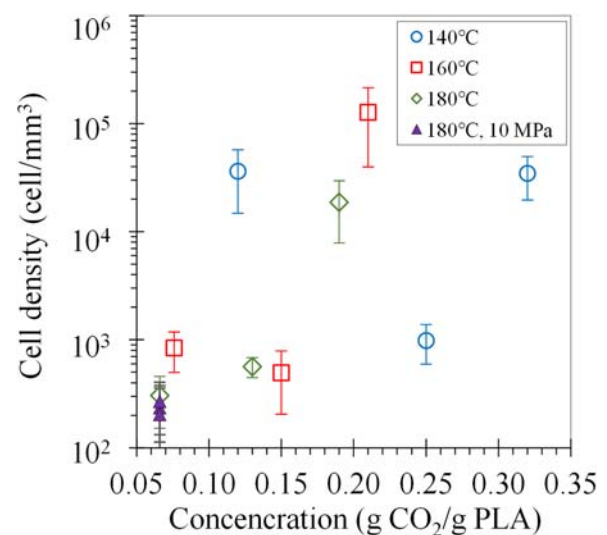


FIG. 28. Effect of CO_2 concentration on cell density. Closed symbols are for data obtained at 180°C and 10 MPa and at various NPDR (3D), and open symbols are for data obtained at NPDR of 0.02 s^{-1} and at various P and T . Error bars represent the standard deviation.

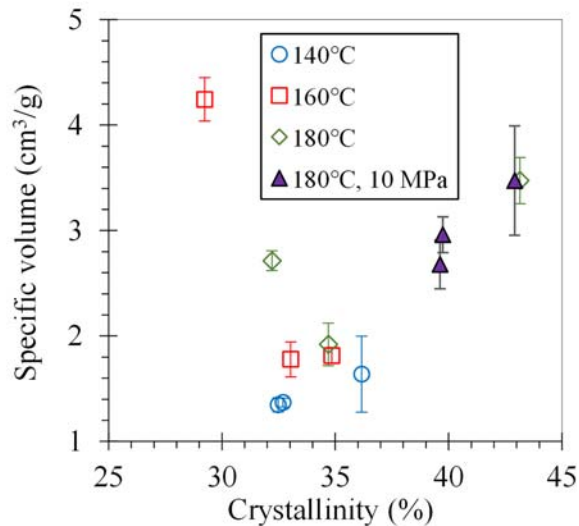


FIG. 29. Effect of crystallinity of foams on specific volume. Closed symbols are the data obtained at $T = 180^\circ\text{C}$ and $P = 10\text{ MPa}$ and at various NPDR (Fig. 21), and open symbols are the data obtained at NPDR = 0.02 s^{-1} and at various pressures and temperatures (Fig. 26). Error bars represent the standard deviation.

Compounded talc (25 wt. %) strongly affects the shear rheology at low frequencies by forming network structures. It was proven that time-temperature superposition was valid at relatively high temperatures, even with upturns in the complex viscosities with decreasing frequencies. The talc particles induce heterogeneous nucleation not only on cells (bubbles), but also on crystal sites that can improve the thermal stability, which is favorable for recycling. Although extensional rheometry portrayed no strain hardening, we were still able to foam the samples and determine the operating windows that can produce various foam structures (conventional and fine-celled foams) for various applications by changing variables. We also compared the effects of the cell expansion during foaming in one-dimensional and three-dimensional environments. The result showed that there was no major difference. However, we evaluated that the concentration of CO_2 in PLA and crystallinity of foams were the two key variables to describe the bulkiness of foams. Surprisingly, the lower the CO_2 concentration, the bulkier the foams at any sorption temperature and pressure.

AUTHORS' CONTRIBUTIONS

L.L. and Y.L. contributed equally to this work.

ACKNOWLEDGMENTS

This study was financially supported by Department of Chemical and Process Engineering, University of Canterbury. We would like to show our gratitude toward the staff in the Department of Chemical and Process Engineering at the University of Canterbury, New Zealand, for their technical and financial support. We also would like to show our gratitude toward Oscar Torres, Kevin Stobbs, and Shaun Mucalo in the Department of Mechanical Engineering at the University of Canterbury, New Zealand, for offering and training the use of DSC, hot press, and SEM, respectively. We are grateful to Lea Maguero at Biopak, Australia for

providing the material information of the PLA cutlery and Roklim Yun at Hisun Korea for supplying the materials and information.

APPENDIX A: NON-STEADY STATE DIFFUSION IN 1D-VERSION 1

There can be two versions of solutions depending on how to set the boundary condition.

The one-dimensional (1D) diffusion through a plane was considered. Due to the PLA sample being thin, assumption of diffusing CO_2 gas only enters through the plane from $z = h$ to $z = 0$, and the diffusion through the edges were negligible. The side view of the PLA sample inside the foaming chamber undergoing one-dimensional diffusion is shown in Fig. 30, and the derivation of the equations is shown below.

In the case for the sorption of carbon dioxide through the plane of PLA sample for the experiment, the PLA sample has a thickness of $z = h$. Given the initial and boundary conditions,

- Initial condition (I.C.): when time $t = 0$, the PLA sample initially possess a uniform concentration. For this case

$$C = C_o = 0 \quad \text{for} \quad 0 \leq z \leq h.$$

- Boundary condition 1 (B.C.1): The carbon dioxide is introduced into the foaming chamber, saturating the top surface of PLA sample when $t > 0$. Therefore

$$C = C_s \quad \text{when} \quad z = h.$$

- Boundary condition 2 (B.C.2): At the bottom surface of PLA sample, the net flux of carbon dioxide is zero. This is due to the foaming chamber wall serving as a barrier that is impermeable to the flux. Therefore

$$\partial C / \partial z = 0, \quad \text{at} \quad z = 0 \quad \text{for} \quad t > 0.$$

To solve this non-steady state diffusion in a plane surface, a dimensionless concentration Y is introduced shown below,

$$Y \equiv \frac{C - C_o}{C_s - C_o}. \quad (\text{A1})$$

The dimensionless concentration Y is introduced and into the transient diffusion in finite 1D medium shown in Eq. (A2). 1-Dimensional diffusion for a plate

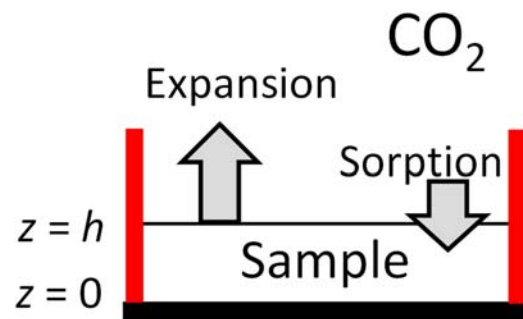


FIG. 30. Side view of PLA sample undergoing 1D diffusion inside the foaming chamber. Diffusion starts at $z = h$ and ends at $z = 0$.

$$\frac{\partial C(z, t)}{\partial t} = D \frac{\partial^2 C(z, t)}{\partial z^2}. \quad (\text{A2})$$

The rewritten 1D transient diffusion equation is shown below,

$$\frac{\partial Y}{\partial t} = D \frac{\partial^2 Y}{\partial z^2}. \quad (\text{A3})$$

Using the dimensionless concentration, the initial and boundary conditions are rewritten and shown below,

- I.C.: for $t = 0$, $Y = 1$ for $0 \leq z \leq h$.
- B.C.1: for $z = h$, $Y = 0$ for $t > 0$.
- Boundary condition 2: for $z = 0$, $\frac{\partial Y}{\partial z} = 0$ for $t > 0$.

Once all the initial and boundary conditions are defined, the separation of variable method was used to derive a general equation,

$$Y(z, t) = T(t)Z(z), \quad (\text{A4})$$

where $T(t)$ only depends on time t and $Z(z)$ only depends on coordinate z , and the partial derivatives are given as

$$\frac{\partial Y}{\partial t} = Z \frac{\partial T}{\partial t}, \quad (\text{A5})$$

$$\frac{\partial Y}{\partial z} = T \frac{\partial^2 Z}{\partial z^2}. \quad (\text{A6})$$

Substituting these two partial derivatives Eqs. (A5) and (A6) shown above into Eq. (A3) and rearrange

$$\begin{aligned} Z \frac{\partial T}{\partial t} &= DT \frac{\partial^2 Z}{\partial z^2}, \\ \frac{1}{DT} \frac{\partial T}{\partial t} &= \frac{1}{Z} \frac{\partial^2 Z}{\partial z^2}. \end{aligned} \quad (\text{A7})$$

The left-hand side of the equation only depends on time t and the right-hand side of the equation depends on coordinate z . As a result, if time t changes, the right-hand side of the equation remains constant and if z coordinate changes, the left-hand side of the equation remains constant. Due to this, the arbitrary negative constant, $-\lambda^2$ can be introduced. (A positive or zero will not give solutions.) This allows the equation to be divided into two separate ordinary differential equations (ODEs) shown in Eqs. (A8) and (A10). Then integrate the ODE separately. The results are shown in Eqs. (A9) and (A11),

$$\frac{1}{DT} \frac{dT}{dt} = -\lambda^2, \quad (\text{A8})$$

$$T(t) = C_1 \exp(-D\lambda^2 t), \quad (\text{A9})$$

$$\frac{1}{Z} \frac{d^2 Z}{dz^2} = -\lambda^2, \quad (\text{A10})$$

$$(z) = C_2 \cos(\lambda z) + C_3 \sin(\lambda z). \quad (\text{A11})$$

Then substituting Eqs. (A9) and (A11) into Eq. (A4) gives

$$Y(z, t) = \exp(-D\lambda^2 t) [C'_1 \cos(\lambda z) + C'_2 \sin(\lambda z)],$$

where $C'_1 = C_1 C_2$ and $C'_2 = C_1 C_3$. These are constants. Since this is a linear equation, the general solution is determined by summing

the solutions of Eq. (A11) by introducing constants A_m and B_m to obtain Eq. (A12)

$$Y(z, t) = \sum_{m=0}^{\infty} \exp(-D\lambda_m^2 t) A_m \cos(\lambda_m z) B_m \sin(\lambda_m z). \quad (\text{A12})$$

In order to use the second boundary condition, Eq. (A12) needs to be differentiated. This is given as Eq. (A13),

$$\frac{\partial Y}{\partial z} = \sum_{m=0}^{\infty} \{ [-\lambda_m A_m \sin(\lambda_m z) + \lambda_m B_m \cos(\lambda_m z)] \exp(-D\lambda_m^2 t) \}. \quad (\text{A13})$$

The boundary and initial conditions are used to determine the arbitrary constants C'_1 and C'_2 .

Using the second boundary condition and Eq. (A13)

- B.C.2: for $z = 0$, $\frac{\partial Y}{\partial z} = 0$ for $t > 0$

$$0 = \sum_{m=0}^{\infty} \{ [-\lambda_m A_m \sin(\lambda_m \times 0) + \lambda_m B_m \cos(\lambda_m \times 0)] \exp(-D\lambda_m^2 t) \},$$

$$\sum_{m=0}^{\infty} \lambda_m B_m \exp(-D\lambda_m^2 t) = 0.$$

Since the exponential part in the equation shown above cannot become zero, the constant B_m has to be zero in order to satisfy the right-hand side of the equation. Therefore

$$B_m = 0. \quad (\text{A14})$$

Using the first boundary condition and Eq. (A13) along with Eq. (A14)

- B.C.1: for $z = h$, $Y = 0$ for $t > 0$

$$0 = \sum_{m=0}^{\infty} \exp(-D\lambda_m^2 t) [A_m \cos(\lambda_m h)].$$

Once again, the exponential decay cannot reach zero. Additionally, A_m cannot be zero either. This is due to if both arbitrary constants equal zero, Eq. (A12) will equal zero

$$\sum_{m=0}^{\infty} [A_m \cos(\lambda_m z)] = 0.$$

Therefore

$$\lambda_m = \frac{(2k+1)\pi}{2h}. \quad (\text{A15})$$

In order to satisfy the second boundary condition, by substituting Eqs. (A14) and (A15) into Eq. (A12), it yields

$$Y(z, t) = \sum_{k=0}^{\infty} \exp \left[-D \left(\frac{(2k+1)\pi}{2h} \right)^2 t \right] A_k \cos \left[\frac{(2k+1)\pi}{2h} z \right]. \quad (\text{A16})$$

Finally, the initial condition is required to determine the constant A_k . Using the initial condition and Eq. (A16)

- I.C.: for $t = 0$, $Y = 1$ for $0 \leq z \leq h$

$$1 = \sum_{k=0}^{\infty} \exp \left[-D \left(\frac{(2k+1)\pi}{2h} \right)^2 \times 0 \right] A_k \cos \left[\frac{(2k+1)\pi}{2h} z \right],$$

$$\sum_{k=0}^{\infty} A_k \cos \left[\frac{(2k+1)\pi}{2h} z \right] = 1. \quad (\text{A17})$$

Multiply both side of Eq. (A17) by Eq. (A18) shown below and integrate from 0 to h ,

$$\cos \frac{(2n+1)\pi z}{2h}. \quad (\text{A18})$$

This yields

$$\int_0^h \cos \frac{(2n+1)\pi z}{2h} dz = \sum_{k=0}^{\infty} A_k \int_0^h \cos \frac{(2k+1)\pi z}{2h} \cos \frac{(2n+1)\pi z}{2h} dz.$$

$$(\text{A19})$$

The left-hand and right-hand side of Eq. (A19) is evaluated separately. For the left-hand side of Eq. (A19). When integrated, it yields

$$\int_0^h \cos \frac{(2n+1)\pi z}{2h} dz = \frac{2h}{(2n+1)\pi} \sin \frac{(2n+1)\pi z}{2h} \Big|_0^h$$

$$= \frac{2h}{(2n+1)\pi} \sin \frac{(2n+1)\pi(h)}{2h}$$

$$- \frac{2h}{(2n+1)\pi} \sin \frac{(2n+1)\pi(0)}{2h}$$

$$= \frac{2h}{(2n+1)\pi} \sin \frac{(2n+1)\pi}{2}. \quad (\text{A20})$$

When $n = 0$

$$\sin \frac{[2(0)+1]\pi}{2} = \sin \left(\frac{\pi}{2} \right) = 1.$$

When $n = 1$

$$\sin \frac{[2(1)+1]\pi}{2} = \sin \left(\frac{3\pi}{2} \right) = -1.$$

When $n = 2$

$$\sin \frac{[2(2)+1]\pi}{2} = \sin \left(\frac{5\pi}{2} \right) = 1.$$

The sine present in Eq. (A20) oscillates between -1 and 1 for any $n > 0$, which is a whole number. Therefore, Eq. (A20) can be generalized into

$$\int_0^h \cos \frac{(2n+1)\pi z}{2h} dz = \frac{2h(-1)^n}{(2n+1)\pi}. \quad (\text{A21})$$

As for the right-hand side of Eq. (A19), first, define new variables shown below

$$a = \frac{\pi}{h} z, \quad (\text{A22})$$

$$b = \frac{2k+1}{2}, \quad (\text{A23})$$

$$c = \frac{2n+1}{2}. \quad (\text{A24})$$

Substitute these new variables into right-hand side of Eq. (19)

$$\int_0^h \cos \frac{(2n+1)\pi z}{2h} dz = \sum_{k=0}^{\infty} A_k \int_0^h \cos(ab) \cos(ac). \quad (\text{A25})$$

Based on orthogonality, shown in Appendix C

$$\sum_{k=0}^{\infty} A_k \int_0^h \cos(ab) \cos(ac) = \begin{cases} \frac{h}{2} & \text{when } n = k, \\ 0 & \text{when } n \neq k. \end{cases}$$

Therefore, due to values of n that does not equal k , making the equation equal 0, the summation sigma is dropped. There is no requirement to add zeros

$$\sum_{k=0}^{\infty} A_k \frac{h}{2} = A_n \frac{h}{2}. \quad (\text{A26})$$

Finally, by making Eq. (A21) equal Eq. (A26) and rearranging this yields

$$\frac{2h(-1)^n}{(2n+1)\pi} = A_n \frac{h}{2},$$

$$A_n = \frac{4(-1)^n}{(2n+1)\pi}. \quad (\text{A27})$$

Substitute Eq. (A27) back into Eq. (A16) to determine the final solution of the problem

$$Y(z, t) = \frac{4}{\pi} \sum_{n=0}^{\infty} \frac{(-1)^n}{2n+1} \exp \left[-D \left(\frac{(2n+1)\pi}{2h} \right)^2 t \right] \cos \frac{(2n+1)\pi z}{2h}.$$

$$(\text{A28})$$

Substituting Eq. (A1) back into Eq. (A28) yields

$$\frac{C(z, t) - C_s}{C_o - C_s} = \frac{4}{\pi} \sum_{n=0}^{\infty} \frac{(-1)^n}{2n+1} \exp \left[-D \left(\frac{(2n+1)\pi}{2h} \right)^2 t \right] \cos \frac{(2n+1)\pi z}{2h}.$$

$$(\text{A29})$$

In order to determine the degree of saturation, Eq. (A29) need to be rearranged. Let

$$x = \frac{4}{\pi} \sum_{n=0}^{\infty} \frac{(-1)^n}{2n+1} \exp \left[-D \left(\frac{(2n+1)\pi}{2h} \right)^2 t \right] \cos \frac{(2n+1)\pi z}{2h}.$$

Therefore

$$\frac{C(z, t) - xC_o}{C_s} = (1 - x).$$

As $C_o = 0$

$$\frac{C(z, t)}{C_s} = 1 - \frac{4}{\pi} \sum_{n=0}^{\infty} \frac{(-1)^n}{2n+1} \exp \left[-D \left(\frac{(2n+1)\pi}{2h} \right)^2 t \right] \cos \frac{(2n+1)\pi z}{2h}.$$

$$(\text{A30})$$

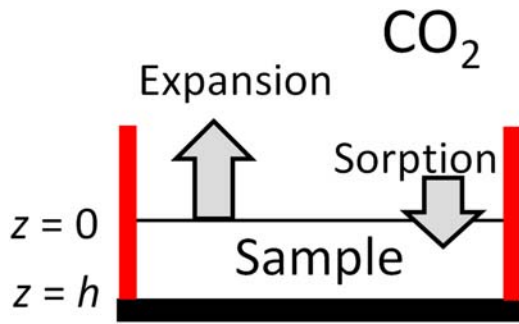


FIG. 31. Side view of PLA sample undergoing 1D diffusion inside the foaming chamber. Diffusion starts at $z = 0$ and ends at $z = h$.

APPENDIX B: NON-STEADY STATE DIFFUSION IN 1D—VERSION 2

The 1D diffusion through a plane was considered. Due to the PLA sample being thin, assumption of diffusing CO_2 gas only enters through the plane from $z = 0$ to $z = h$ and the diffusion through the edges were negligible. The side view of the PLA sample inside the foaming chamber undergoing one-dimensional diffusion is shown in Fig. 31, and the derivation of the equations is shown below.

In the case for the sorption of carbon dioxide through the plane of PLA sample for the experiment, the PLA sample has a thickness of $z = h$.

Given the initial and boundary conditions:

- Initial condition (I.C.): when time $t = 0$, the PLA sample initially possess a uniform concentration. For this case

$$C = C_o = 0 \text{ for } 0 \leq z \leq h.$$

- Boundary condition 1 (B.C.1): The carbon dioxide is introduced into the foaming chamber, saturating the top surface of PLA sample when $t > 0$. Therefore

$$C = C_s \text{ when } z = 0.$$

- Boundary condition 2 (B.C.2): At the bottom surface of PLA sample, the net flux of carbon dioxide is zero. This is due to the foaming chamber wall serving as a barrier that is impermeable to the flux. Therefore

$$\frac{\partial C}{\partial z} = 0, \text{ at } z = h$$

for

$$t > 0.$$

To solve this non-steady state diffusion in a plane surface, a dimensionless concentration Y is introduced below

$$Y \equiv \frac{C - C_o}{C_s - C_o}. \quad (\text{B1})$$

The dimensionless concentration Y is introduced and into the transient diffusion in finite 1D medium shown in Eq. (B2).

1D diffusion for a plate

$$\frac{\partial C(z, t)}{\partial t} = D \frac{\partial^2 C(z, t)}{\partial z^2}. \quad (\text{B2})$$

The rewritten 1-D transient diffusion equation is shown below

$$\frac{\partial Y}{\partial t} = D \frac{\partial^2 Y}{\partial z^2}. \quad (\text{B3})$$

Using the dimensionless concentration, the initial and boundary conditions are rewritten and shown below as

The initial and boundary conditions are shown below

- I.C.: for $t = 0$, $Y = 1$ for $0 \leq z \leq h$.
- B.C.1: for $z = 0$, $Y = 0$ for $t > 0$.
- B.C.2: for $z = h$, $\frac{\partial Y}{\partial z} = 0$ for $t > 0$.

Once all the initial and boundary conditions are defined, the separation of variable method was used to derive a general equation

$$Y(z, t) = T(t)Z(z), \quad (\text{B4})$$

where the $T(t)$ only depends on time t and $Z(z)$ only depends on coordinate z , the partial derivatives are given as

$$\frac{\partial Y}{\partial t} = Z \frac{\partial T}{\partial t}, \quad (\text{B5})$$

$$\frac{\partial Y}{\partial z} = T \frac{\partial^2 Z}{\partial z^2}. \quad (\text{B6})$$

Substituting these two partial derivatives Eqs. (B5) and (B6) shown above, into Eq. (B3) and rearrange

$$\begin{aligned} Z \frac{\partial T}{\partial t} &= DT \frac{\partial^2 Z}{\partial z^2}, \\ \frac{1}{DT} \frac{\partial T}{\partial t} &= \frac{1}{Z} \frac{\partial^2 Z}{\partial z^2}. \end{aligned} \quad (\text{B7})$$

The left-hand side of Eq. (B7) only depends on time t and the right-hand side of the equation depends on coordinate z . As a result, if time t changes, the right-hand side of the equation remains constant and if z coordinate changes, the left-hand side of the equation remain constant. Due to this, the arbitrary negative constant, $-\lambda^2$ can be introduced. (A positive or zero will not give solutions.) This allows the equation to be divided into two separate ordinary differential equations (ODEs) shown in Eqs. (B8) and (B10). Then integrate the ODEs separately. The results are shown in Eqs. (B9) and (B11)

$$\frac{1}{DT} \frac{dT}{dt} = -\lambda^2, \quad (\text{B8})$$

$$T(t) = C_1 \exp(-D\lambda^2 t), \quad (\text{B9})$$

$$\frac{1}{Z} \frac{d^2 Z}{dz^2} = -\lambda^2, \quad (\text{B10})$$

$$Z(z) = C_2 \cos(\lambda z) + C_3 \sin(\lambda z). \quad (\text{B11})$$

Then substitute Eqs. (B9) and (B11) into Eq. (B4)

$$Y(z, t) = \exp(-D\lambda^2 t) [C'_1 \cos(\lambda z) + C'_2 \sin(\lambda z)],$$

where $C'_1 = C_1 C_2$ and $C'_2 = C_1 C_3$, and these are constants.

Since this is a linear equation, the general solution is determined by summing the solutions of Eq. (B11) by introducing constants A_m and B_m to obtain Eq. (B12)

$$Y(z, t) = \sum_{m=0}^{\infty} \exp(-D\lambda_m^2 t) A_m \cos(\lambda_m z) B_m \sin(\lambda_m z). \quad (\text{B12})$$

In order to use the second boundary condition, Eq. (B12) need to be differentiated. This is given as

$$\frac{\partial Y}{\partial z} = \sum_{m=0}^{\infty} \{ [-\lambda_m A_m \sin(\lambda_m z) + \lambda_m B_m \cos(\lambda_m z)] \exp(-D\lambda_m^2 t) \}. \quad (\text{B13})$$

The boundary and initial conditions are used to determine the arbitrary constants C_1 and C_2 .

Using the first boundary condition and Eq. (B12)

- B.C.1: for $z = 0$, $Y = 0$ for $t > 0$

$$0 = \sum_{m=0}^{\infty} \exp(-D\lambda_m^2 t) A_m \cos(\lambda_m \times 0) B_m \sin(\lambda_m \times 0),$$

$$0 = \sum_{m=0}^{\infty} \exp(-D\lambda_m^2 t) A_m.$$

Since the exponential part in the equation shown above cannot become zero, the constant A_m has to be zero in order to satisfy the right-hand side of the equation. Therefore

$$A_m = 0. \quad (\text{B14})$$

Using the second boundary condition and Eq. (B13) along Eq. (B14)

- B.C.2: for $z = h$, $\frac{\partial Y}{\partial z} = 0$ for $t > 0$

$$0 = \sum_{m=0}^{\infty} \left[[-\lambda_m(0) \sin(\lambda_m h) + \lambda_m B_m \cos(\lambda_m h)] \exp(-D\lambda_m^2 t) \right],$$

$$0 = \sum_{m=0}^{\infty} [\lambda_m B_m \cos(\lambda_m h) \exp(-D\lambda_m^2 t)].$$

Once again, the exponential decay cannot reach zero. Additionally, B_m cannot be zero either. This is due to, if both arbitrary constants equal zero, the entire general equation (B12) will equal zero. Therefore

$$\lambda_m = \frac{(2k+1)\pi}{2h}. \quad (\text{B15})$$

In order to satisfy the second boundary condition. By substituting Eqs. (B14) and (B15) into Eq. (B12), it yields

$$Y(z, t) = \sum_{m=0}^{\infty} \exp \left[-D \left(\frac{(2k+1)\pi}{2h} \right)^2 t \right] \times \left\{ 0 \times \cos \left[\frac{(2k+1)\pi}{2h} z \right] + B_k \sin \frac{(2k+1)\pi z}{2h} \right\},$$

$$Y(z, t) = \sum_{k=0}^{\infty} B_k \sin \frac{(2k+1)\pi z}{2h} \exp \left[-D \left(\frac{(2k+1)\pi}{2h} \right)^2 t \right]. \quad (\text{B16})$$

Finally, the initial condition is required to determine the constant B_k . Using the initial condition and Eq. (B16)

- I.C.: for $t = 0$, $Y = 1$ for $0 \leq z \leq h$

$$1 = \sum_{k=0}^{\infty} B_k \sin \frac{(2k+1)\pi z}{2h} \exp \left[-D \left(\frac{(2k+1)\pi}{2h} \right)^2 (0) \right],$$

$$1 = \sum_{k=0}^{\infty} B_k \sin \frac{(2k+1)\pi z}{2h}. \quad (\text{B17})$$

Multiply both side of Eq. (B17) by Eq. (B18) shown below and integrate from 0 to h,

$$\sin \frac{(2n+1)\pi z}{2h}. \quad (\text{B18})$$

This yields

$$\int_0^h \sin \frac{(2n+1)\pi z}{2h} dz = \sum_{k=0}^{\infty} B_k \int_0^h \sin \frac{(2k+1)\pi z}{2h} \sin \frac{(2n+1)\pi z}{2h} dz. \quad (\text{B19})$$

The left- and right-hand sides of Eq. (B19) are evaluated separately. For the left-hand side of Eq. (B19), when integrated, it yields

$$\int_0^h \sin \frac{(2n+1)\pi z}{2h} dz$$

$$= -\frac{2h}{(2n+1)\pi} \cos \frac{(2n+1)\pi z}{2h} \Big|_0^h$$

$$= \left[-\frac{2h}{(2n+1)\pi} \cos \frac{(2n+1)\pi h}{2h} \right] - \left[-\frac{2h}{(2n+1)\pi} \cos \frac{0}{2h} \right]$$

$$= \left[-\frac{2h}{(2n+1)\pi} \cos \frac{(2n+1)\pi}{2} \right] + \frac{2h}{(2n+1)\pi}$$

$$= -\frac{2h}{(2n+1)\pi} \left[\cos \frac{(2n+1)\pi}{2} - 1 \right]. \quad (\text{B20})$$

When $n = 0$

$$\left[\cos \frac{(0+1)\pi}{2} - 1 \right] = \cos \left(\frac{\pi}{2} \right) - 1 = -1.$$

When $n = 1$

$$\left[\cos \frac{(2+1)\pi}{2} - 1 \right] = \cos \left(\frac{3\pi}{2} \right) - 1 = -1.$$

When $n = 2$

$$\left[\cos \frac{(4+1)\pi}{2} - 1 \right] = \cos \left(\frac{5\pi}{2} \right) - 1 = -1.$$

The cosine present in Eq. (B20) equals -1 for any $n > 0$, which is a whole number. Therefore, Eq. (B20) can be generalized into

$$\int_0^h \sin \frac{(2n+1)\pi z}{2h} dz = \frac{2h}{(2n+1)\pi}. \quad (\text{B21})$$

As for the right-hand side of Eq. (B19), first define new variables shown as

$$a = \frac{\pi}{h}z, \quad (\text{B22})$$

$$b = \frac{2k+1}{2}, \quad (\text{B23})$$

$$c = \frac{2n+1}{2}. \quad (\text{B24})$$

Substitute these new variables into right-hand side of Eq. (19),

$$\begin{aligned} \sum_{k=0}^{\infty} B_{sk} \int_0^h \sin \frac{(2k+1)\pi z}{2h} \sin \frac{(2n+1)\pi z}{2h} \\ = \sum_{k=0}^{\infty} B_{sk} \int_0^h \sin(ab) \sin(ac). \end{aligned} \quad (\text{B25})$$

Based on orthogonality, shown in Appendix D

$$\sum_{k=0}^{\infty} B_k \int_0^h \sin(ab) \sin(ac) = \begin{cases} \frac{h}{2} & \text{when } n = k, \\ 0 & \text{when } n \neq k. \end{cases}$$

Therefore, due to values of n that does not equal k , making the equation equal 0, the summation sigma is dropped. There is no requirement to add zeros

$$\sum_{k=0}^{\infty} B_k \frac{h}{2} = B_n \frac{h}{2}. \quad (\text{B26})$$

Finally, by making Eq. (B21) equal Eq. (B26) and rearranging this yield Eq. (B27),

$$\begin{aligned} \frac{2h}{(2n+1)\pi} &= B_n \frac{h}{2}, \\ B_n &= \frac{4}{(2n+1)\pi}. \end{aligned} \quad (\text{B27})$$

Substitute Eq. (B27) back into Eq. (B16) to determine the final solution of the problem,

$$Y(z, t) = \frac{4}{\pi} \sum_{n=0}^{\infty} \frac{1}{2n+1} \exp \left[-D \left(\frac{(2n+1)\pi}{2h} \right)^2 t \right] \sin \frac{(2n+1)\pi z}{2h}. \quad (\text{B28})$$

Substituting Eq. (B1) back into Eq. (B28) yields

$$\frac{C(z, t) - C_s}{C_o - C_s} = \frac{4}{\pi} \sum_{n=0}^{\infty} \frac{1}{2n+1} \exp \left[-D \left(\frac{(2n+1)\pi}{2h} \right)^2 t \right] \sin \frac{(2n+1)\pi z}{2h}. \quad (\text{B29})$$

In order to determine the degree of saturation, Eq. (B29) needs to be rearranged. Let

$$x = \frac{4}{\pi} \sum_{n=0}^{\infty} \frac{1}{2n+1} \exp \left[-D \left(\frac{(2n+1)\pi}{2h} \right)^2 t \right] \sin \frac{(2n+1)\pi z}{2h}.$$

Therefore

$$\frac{C(z, t) - xC_o}{C_s} = (1 - x).$$

As $C_o = 0$ as the initial condition

$$\frac{C(z, t)}{C_s} = 1 - \frac{4}{\pi} \sum_{n=0}^{\infty} \frac{1}{2n+1} \exp \left[-D \left(\frac{(2n+1)\pi}{2h} \right)^2 t \right] \sin \frac{(2n+1)\pi z}{2h}. \quad (\text{B30})$$

APPENDIX C: ORTHOGONALITY FOR THE COSINE FUNCTION

Definition of orthogonal function:

The two non-zero functions, $f(x)$ and $g(x)$ are considered to be orthogonal on $a \leq x \leq b$ if

$$\int_a^b f(x)g(x)dx = 0. \quad (\text{C1})$$

If a set of non-zero functions, $\{f_i(x)\}$ on $a \leq x \leq b$ are orthogonal for every $i \neq j$, then it is considered to be mutually orthogonal,

$$\int_a^b f_i(x)f_j(x)dx = \begin{cases} 0 & i \neq j, \\ c & i = j. \end{cases} \quad (\text{C2})$$

The useful trigonometric formula needed for integration are shown below,

$$\sin \alpha \cos \beta = \frac{1}{2} [\sin(\alpha - \beta) + \sin(\alpha + \beta)], \quad (\text{C3})$$

$$\sin \alpha \sin \beta = \frac{1}{2} [\cos(\alpha - \beta) - \cos(\alpha + \beta)], \quad (\text{C4})$$

$$\cos \alpha \cos \beta = \frac{1}{2} [\cos(\alpha - \beta) + \cos(\alpha + \beta)]. \quad (\text{C5})$$

For cosine function given as

$$\cos(mx). \quad (\text{C6})$$

Multiply Eq. (C6) by

$$\cos(nx). \quad (\text{C7})$$

This yields

$$\int_0^\pi [\cos(mx)\cos(nx)]dx. \quad (\text{C8})$$

• For the case when

$$n = m.$$

Then

$$\int_0^\pi [\cos(mx)\cos(nx)]dx = \int_0^\pi \cos^2(mx)dx. \quad (C9)$$

From the trigonometric formula

$$\cos^2(\alpha) = \frac{1 + \cos(2\alpha)}{2}. \quad (C10)$$

Using Eq. (C10), Eq. (C9) can be rewritten as

$$\frac{1}{2} \int_0^\pi [1 + \cos(2mx)]dx. \quad (C11)$$

Now integrate from 0 to π . This yields

$$\begin{aligned} &= \frac{1}{2} \left[x + \frac{1}{2m} \sin(2mx) \right]_0^\pi \\ &= \frac{1}{2} \left[\pi + \frac{1}{2m} \sin(2m\pi) \right]. \end{aligned}$$

For integer $n = m$ and $m = 0$ to ∞ the $\sin(2m\pi)$ will always equal 0. Therefore

$$\int_0^\pi [\cos(mx)\cos(nx)]dx = \frac{\pi}{2}. \quad (C12)$$

• For the case when

$$n \neq m.$$

Using Eq. (C5), Eq. (C9) can be rewritten in the form of

$$\frac{1}{2} \int_0^\pi [\cos((m-n)x) + \cos((m+n)x)]dx. \quad (C13)$$

Integrating Eq. (C13) gives

$$\begin{aligned} &\frac{1}{2} \left[\frac{1}{m-n} \sin((m-n)x) + \frac{1}{m+n} \sin((m+n)x) \right]_0^\pi \\ &= \frac{1}{2} \left[\frac{1}{m-n} \sin((m-n)\pi) + \frac{1}{m+n} \sin((m+n)\pi) \right]. \end{aligned} \quad (C14)$$

As long as $n \neq m$, Eq. (C14) will always equal 0,

$$\frac{1}{2} \left[\frac{1}{m-n} \sin(m-n)\pi + \frac{1}{m+n} \sin(m+n)\pi \right] = 0 \text{ for } n \neq m. \quad (C15)$$

From the results from Eqs. (C12) and (C15), the orthogonality of cosine is shown below,

$$\int_a^b [\cos(mx)\cos(nx)]dx = \begin{cases} 0 & m \neq n, \\ c > 0 & n = m. \end{cases} \quad (C16)$$

APPENDIX D: ORTHOGONALITY FOR THE SINE FUNCTION

For the sine function given as

$$\sin(mx). \quad (D1)$$

Multiply Eq. (D1) by

$$\sin(nx). \quad (D2)$$

This yields

$$\int_0^\pi [\sin(mx)\sin(nx)]dx. \quad (D3)$$

• For the case when

$$n = m.$$

Equation (D3) becomes

$$\int_0^\pi [\sin^2(mx)]dx. \quad (D4)$$

Using the trigonometric formula shown below,

$$\sin^2(\alpha) = \frac{1 - \cos(2\alpha)}{2}. \quad (D5)$$

Equation (D4) can be rewritten as

$$\frac{1}{2} \int_0^\pi [1 - \cos(2mx)]dx. \quad (D6)$$

Integrating Eq. (D6) yields

$$\begin{aligned} &\frac{1}{2} \left[x - \frac{1}{2m} \sin(2mx) \right]_0^\pi \\ &= \frac{1}{2} \left[\pi - \frac{1}{2m} \sin(2m\pi) \right]. \end{aligned} \quad (D7)$$

For integer $n = m$ and $m = 0$ to ∞ the $\sin(2m\pi)$ will always equal 0. Therefore

$$\int_0^\pi [\sin(mx)\sin(nx)]dx = \frac{\pi}{2}. \quad (D8)$$

• For the case when

$$n \neq m.$$

Using Eq. (C4), Eq. (D3) can be rewritten in the form of

$$\frac{1}{2} \int_0^\pi [\cos((m-n)x) - \cos((m+n)x)]dx. \quad (D9)$$

Integrating Eq. (D9) gives

$$\begin{aligned} &\frac{1}{2} \left[\frac{1}{m-n} \sin((m-n)x) - \frac{1}{m+n} \sin((m+n)x) \right]_0^\pi \\ &= \frac{1}{2} \left[\frac{1}{m-n} \sin((m-n)\pi) - \frac{1}{m+n} \sin((m+n)\pi) \right]. \end{aligned} \quad (D10)$$

As long as $n \neq m$, Eq. (D10) will always equal 0,

$$\frac{1}{2} \left[\frac{1}{m-n} \sin(m-n)\pi + \frac{1}{m+n} \sin(m+n)\pi \right] = 0 \text{ for } n \neq m. \quad (D11)$$

From using the results from Eqs. (D8) and (D11), the orthogonality of sine function is shown below,

$$\int_a^b [\sin(mx)\sin(nx)]dx = \begin{cases} 0 & m \neq n, \\ c > 0 & n = m. \end{cases} \quad (\text{D12})$$

DATA AVAILABILITY

The data that support the findings of this study are available from the corresponding author upon reasonable request.

REFERENCES

- ¹X. Quecholac-Piña, M. d. C. Hernández-Berriel, M. d. C. Mañón-Salas, R. M. Espinosa-Valdemar, and A. Vázquez-Morillas, "Degradation of plastics under anaerobic conditions: A short review," *Polymers* **12**(1), 109 (2020).
- ²J. A. Glaser, "Biological degradation of polymers in the environment," in *Plastics in the Environment* (IntechOpen, 2019).
- ³A. Chamas *et al.*, "Degradation rates of plastics in the environment," *ACS Sustainable Chem. Eng.* **8**(9), 3494–3511 (2020).
- ⁴J. Sills and T. M. Adyel, "Accumulation of plastic waste during COVID-19," *Science* **369**(6509), 1314–1315 (2020).
- ⁵J. Xi, X. A. Si, and R. Nagarajan, "Effects of mask-wearing on the inhalability and deposition of airborne SARS-CoV-2 aerosols in human upper airway," *Phys. Fluids* **32**(12), 123312 (2020).
- ⁶J. Hopewell, R. Dvorak, and E. Kosior, "Plastics recycling: Challenges and opportunities," *Philos. Trans. R. Soc., B* **364**(1526), 2115–2126 (2009).
- ⁷A. L. Patrício Silva *et al.*, "Increased plastic pollution due to COVID-19 pandemic: Challenges and recommendations," *Chem. Eng. J.* **405**, 126683 (2021).
- ⁸A. Lendlein and A. Sisson, *Handbook of Biodegradable Polymers* (Wiley, 2011).
- ⁹J. P. Harrison, C. Boardman, K. O'Callaghan, A.-M. Delort, and J. Song, "Biodegradability standards for carrier bags and plastic films in aquatic environments: A critical review," *R. Soc. Open Sci.* **5**(5), 171792 (2018).
- ¹⁰F. Degli Innocenti and T. Breton, "Intrinsic biodegradability of plastics and ecological risk in the case of leakage," *ACS Sustainable Chem. Eng.* **8**(25), 9239–9249 (2020).
- ¹¹A. Jiménez, M. Peltzer, and R. Ruseckaite, *Poly(Lactic Acid) Science and Technology, Polymer Chemistry Series* (RCS, Cambridge, 2014).
- ¹²T. S. B. Lee and S. Tuen, *Poly(lactic Acid): A Practical Guide for the Processing, Manufacturing, and Applications of PLA*, 2nd ed. (Elsevier, Oxford, 2019).
- ¹³B. Kalb and A. J. Pennings, "General crystallization behaviour of poly(l-lactic acid)," *Polymer* **21**(6), 607–612 (1980).
- ¹⁴Y. Ikada, K. Jamshidi, H. Tsuji, and S. H. Hyon, "Stereocomplex formation between enantiomeric poly(lactides)," *Macromolecules* **20**(4), 904–906 (1987).
- ¹⁵S. Saeidlou, M. A. Huneault, H. Li, P. Sammut, and C. B. Park, "Evidence of a dual network/spherulitic crystalline morphology in PLA stereocomplexes," *Polymer* **53**(25), 5816–5824 (2012).
- ¹⁶A. Michalski, T. Makowski, T. Biedroń, M. Brzeziński, and T. Biela, "Controlling polylactide stereocomplex (sc-PLA) self-assembly: From microspheres to nanoparticles," *Polymer* **90**, 242–248 (2016).
- ¹⁷H. J. Lehermeier and J. R. Dorgan, "Melt rheology of poly(lactic acid): Consequences of blending chain architectures," *Polym. Eng. Sci.* **41**(12), 2172–2184 (2001).
- ¹⁸J. R. Dorgan, J. Janzen, M. P. Clayton, S. B. Hait, and D. M. Knauss, "Melt rheology of variable L-content poly(lactic acid)," *J. Rheol.* **49**(3), 607–619 (2005).
- ¹⁹N. Othman, C. Xu, P. Mehrkhodavandi, and S. G. Hatzikiriakos, "Thermorheological and mechanical behavior of polylactide and its enantiomeric diblock copolymers and blends," *Polymer* **53**(12), 2443–2452 (2012).
- ²⁰M. Nofar, R. Salehiyan, and S. Sinha Ray, "Rheology of poly(lactic acid)-based systems," *Polym. Rev.* **59**(3), 465–509 (2019).
- ²¹J. Wang, W. Zhu, H. Zhang, and C. B. Park, "Continuous processing of low-density, microcellular poly(lactic acid) foams with controlled cell morphology and crystallinity," *Chem. Eng. Sci.* **75**, 390–399 (2012).
- ²²M. Nofar and C. B. Park, "Poly(lactic acid) foaming," *Prog. Polym. Sci.* **39**(10), 1721–1741 (2014).
- ²³J. M. Julien, J. C. Quantin, J. C. Bénézet, A. Bergeret, M. F. Lacrampe, and P. Krawczak, "Chemical foaming extrusion of poly(lactic acid) with chain-extenders: Physical and morphological characterizations," *Eur. Polym. J.* **67**, 40–49 (2015).
- ²⁴A. Tabatabaei and C. B. Park, "In situ visualization of PLA crystallization and crystal effects on foaming in extrusion," *Eur. Polym. J.* **96**, 505–519 (2017).
- ²⁵Y. Yang *et al.*, "Foaming of poly(lactic acid) with supercritical CO₂: The combined effect of crystallinity and crystalline morphology on cellular structure," *J. Supercrit. Fluids* **145**, 122–132 (2019).
- ²⁶M. F. Cosate de Andrade, P. M. S. Souza, O. Cavalett, and A. R. Morales, "Life cycle assessment of poly(lactic acid) (PLA): Comparison between chemical recycling, mechanical recycling and composting," *J. Polym. Environ.* **24**(4), 372–384 (2016).
- ²⁷P. McKeown and M. D. Jones, "The chemical recycling of PLA: A review," *Sustainable Chem.* **1**(1), 1–22 (2020).
- ²⁸E. O. Cisneros-López *et al.*, "Recycled poly(lactic acid)-based 3D printed sustainable biocomposites: A comparative study with injection molding," *Mater. Today Sustainability* **78**, 100027 (2020).
- ²⁹D. Garlotta, "A literature review of poly(lactic acid)," *J. Polym. Environ.* **9**(2), 63–84 (2001).
- ³⁰M. Cristea, D. Ionita, and M. M. Iftime, "Dynamic mechanical analysis investigations of PLA-based renewable materials: How are they useful?," *Materials* **13**(22), 5302 (2020).
- ³¹M. L. Di Lorenzo and R. Androsch, *Industrial Applications of Poly(Lactic Acid)*, Advances in Polymer Science (Springer, 2018).
- ³²K. Madhavan Nampoothiri, N. R. Nair, and R. P. John, "An overview of the recent developments in polylactide (PLA) research," *Bioresour. Technol.* **101**(22), 8493–8501 (2010).
- ³³J. Ren, *Biodegradable Poly(Lactic Acid): Synthesis, Modification, Processing and Applications* (Springer, 2011).
- ³⁴R. Auras, B. Harte, and S. Selke, "An overview of polylactides as packaging materials," *Macromol. Biosci.* **4**(9), 835–864 (2004).
- ³⁵T. Casalini, F. Rossi, A. Castrovinci, and G. Perale, "A perspective on polylactide acid-based polymers use for nanoparticles synthesis and applications," *Front. Bioeng. Biotechnol.* **7**, 259 (2019).
- ³⁶M. Murariu and P. Dubois, "PLA composites: From production to properties," *Adv. Drug Delivery Rev.* **107**, 17–46 (2016).
- ³⁷D. E. Henton, P. Gruber, J. Lunt, and J. Randall, "Polylactic acid technology," in *Natural Fibers, Biopolymers, and Biocomposites*, 1st ed., edited by A. K. Mohanty, M. Misra, and L. T. Drzal (CRC Press, Boca Raton, 2005), see https://www.amazon.com/Natural-Fibers-Biopolymers-Biocomposites-Mohanty/dp/084931741X/ref=sr_1_1?dchild=1&keywords=Natural+Fibers%2C+Biopolymers%2C+and+Biocomposites&qid=1623068419&sr=8-1.
- ³⁸R. Auras, L.-T. Lim, S. E. M. Selke, and H. Tsuji, *Poly(Lactic Acid)* (Wiley, 2010).
- ³⁹L. T. Sin and B. S. Tuen, *Poly(lactic Acid): A Practical Guide for the Processing, Manufacturing, and Applications of PLA*, 2nd ed., Poly(lactic Acid) (Elsevier, Oxford, 2019).
- ⁴⁰M. Nofar and C. B. Park, *Polylactide Foams: Fundamentals, Manufacturing, and Applications* (Elsevier, Oxford, 2018), pp. 17–34.
- ⁴¹L. T. Lim, R. Auras, and M. Rubino, "Processing technologies for poly(lactic acid)," *Prog. Polym. Sci.* **33**(8), 820–852 (2008).
- ⁴²M. L. Di Lorenzo and R. Androsch, *Synthesis, Structure and Properties of Poly(Lactic Acid)*, Advances in Polymer Science (Springer, 2018).
- ⁴³N. Weingart, D. Raps, M. Lu, L. Endner, and V. Altstädt, "Comparison of the foamability of linear and long-chain branched polypropylene—The legend of strain-hardening as a requirement for good foamability," *Polymers* **12**(3), 725 (2020).
- ⁴⁴M. R. Snowdon, F. Wu, A. K. Mohanty, and M. Misra, "Comparative study of the extrinsic properties of poly(lactic acid)-based biocomposites filled with talc versus sustainable biocarbon," *RSC Adv.* **9**(12), 6752–6761 (2019).
- ⁴⁵Y.-P. Song, D.-Y. Wang, X.-L. Wang, L. Lin, and Y.-Z. Wang, "A method for simultaneously improving the flame retardancy and toughness of PLA," *Polym. Adv. Technol.* **22**(12), 2295–2301 (2011).

- ⁴⁶F. Yu, T. Liu, X. Zhao, X. Yu, A. Lu, and J. Wang, "Effects of talc on the mechanical and thermal properties of polylactide," *J. Appl. Polym. Sci.* **125** (S2), E99–E109 (2012).
- ⁴⁷A. M. Harris and E. C. Lee, "Improving mechanical performance of injection molded PLA by controlling crystallinity," *J. Appl. Polym. Sci.* **107**(4), 2246–2255 (2008).
- ⁴⁸X. Liu, X. Liu, and Y. Hu, "Investigation of the thermal decomposition of talc," *Clays Clay Miner.* **62**(2), 137–144 (2014).
- ⁴⁹L. Cui, Y. Wang, R. Zhang, and Y. Liu, "Design high heat-resistant stereocomplex poly(lactide acid) by cross-linking and plasticizing," *Adv. Polym. Technol.* **37**(7), 2429–2435 (2018).
- ⁵⁰N. S. Oliveira, J. Dorgan, J. A. P. Coutinho, A. Ferreira, J. L. Daridon, and I. M. Marrucho, "Gas solubility of carbon dioxide in poly(lactic acid) at high pressures," *J. Polym. Sci., Part B: Polym. Phys.* **44**(6), 1010–1019 (2006).
- ⁵¹N. S. Oliveira, J. Oliveira, T. Gomes, A. Ferreira, J. Dorgan, and I. M. Marrucho, "Gas sorption in poly(lactic acid) and packaging materials," *Fluid Phase Equilib.* **222223**, 317–324 (2004).
- ⁵²L. Bao, J. R. Dorgan, D. Knauss, S. Hait, N. S. Oliveira, and I. M. Marrucho, "Gas permeation properties of poly(lactic acid) revisited," *J. Membr. Sci.* **285** (1–2), 166–172 (2006).
- ⁵³J. R. Rocca-Smith *et al.*, "How high pressure CO₂ impacts PLA film properties," *eXPRESS Polym. Lett.* **11**(4), 320–333 (2017).
- ⁵⁴G. Li, H. Li, L. S. Turng, S. Gong, and C. Zhang, "Measurement of gas solubility and diffusivity in polylactide," *Fluid Phase Equilib.* **246**(1–2), 158–166 (2006).
- ⁵⁵S. H. Mahmood, M. Keshtkar, and C. B. Park, "Determination of carbon dioxide solubility in polylactide acid with accurate PVT properties," *J. Chem. Thermodyn.* **70**, 13–23 (2014).
- ⁵⁶H. E. Park and J. M. Dealy, "Effects of pressure and supercritical fluids on the viscosity of polyethylene," *Macromolecules* **39**(16), 5438–5452 (2006).
- ⁵⁷I. C. Sanchez and R. H. Lacombe, "An elementary molecular theory of classical fluids. Pure fluids," *J. Phys. Chem.* **80**(21), 2352–2362 (1976).
- ⁵⁸I. C. Sanchez and R. H. Lacombe, "Statistical thermodynamics of polymer solutions," *Macromolecules* **11**(6), 1145–1156 (1978).
- ⁵⁹M. B. Kiszka, M. A. Meilchen, and M. A. McHugh, "Modeling high-pressure gas-polymer mixtures using the Sanchez-Lacombe equation of state," *J. Appl. Polym. Sci.* **36**(3), 583–597 (1988).
- ⁶⁰G. Li, J. Wang, C. B. Park, and R. Simha, "Measurement of gas solubility in linear/branched PP melts," *J. Polym. Sci., Part B: Polym. Phys.* **45**(17), 2497–2508 (2007).
- ⁶¹R. Simha and T. Somcynsky, "On the statistical thermodynamics of spherical and chain molecule fluids," *Macromolecules* **2**(4), 342–350 (1969).
- ⁶²R. K. Jain and R. Simha, "Statistical thermodynamics of multicomponent fluids. 2. Equation of state and phase relations," *Macromolecules* **17**(12), 2663–2668 (1984).
- ⁶³Y. G. Li, C. B. Park, H. B. Li, and J. Wang, "Measurement of the PVT property of PP/CO₂ solution," *Fluid Phase Equilib.* **270**(1–2), 15–22 (2008).
- ⁶⁴K. Sarikhani, K. Jeddi, R. B. Thompson, C. B. Park, and P. Chen, "Effect of pressure and temperature on interfacial tension of poly lactic acid melt in supercritical carbon dioxide," *Thermochim. Acta* **609**, 1–6 (2015).
- ⁶⁵Y. G. Li, S. H. Mahmood, and C. B. Park, "Visualization for measuring the PVT property of viscoelastic polystyrene/CO₂ mixtures at elevated temperatures and pressures," *Polym. Test.* **55**, 88–96 (2016).
- ⁶⁶A. Phan, D. Fan, and A. Striolo, "Fluid transport through heterogeneous pore matrices: Multiscale simulation approaches," *Phys. Fluids* **32**(10), 101301 (2020).
- ⁶⁷L. M. Matuana, "Foaming," in *Poly(Lactic Acid): Synthesis, Structures, Properties, Processing, and Applications*, edited by R. A. Auras, L.-T. S. Lim, E. M. Susan, and H. Tsuji (Wiley, 2010), pp. 273–291.
- ⁶⁸E. S. Kim, H. E. Park, C. R. Lopez-Barron, and P. C. Lee, "Enhanced foamability with shrinking microfibrils in linear polymer," *Polymers* **11**(2), 211 (2019).
- ⁶⁹V. Speranza, A. D. Meo, and R. Pantani, "Thermal and hydrolytic degradation kinetics of PLA in the molten state," *Polym. Degrad. Stab.* **100**, 37–41 (2014).
- ⁷⁰H. E. Park, S. T. Lim, H. M. Laun, and J. M. Dealy, "Measurement of pressure coefficient of melt viscosity: Drag flow versus capillary flow," *Rheol. Acta* **47** (9), 1023–1038 (2008).
- ⁷¹S. W. Li, H. E. Park, and J. M. Dealy, "Evaluation of molecular linear viscoelastic models for polydisperse H polybutadienes," *J. Rheol.* **55**(6), 1341–1373 (2011).
- ⁷²N. M. Rudolph, A. C. Agudelo, J. C. Granada, H. E. Park, and T. A. Osswald, "WLF model for the pressure dependence of zero shear viscosity of polycarbonate," *Rheol. Acta* **55**(8), 673–681 (2016).
- ⁷³H. E. Park, J. M. Dealy, G. R. Marchand, J. Wang, S. Li, and R. A. Register, "Rheology and structure of molten, olefin multiblock copolymers," *Macromolecules* **43**(16), 6789–6799 (2010).
- ⁷⁴R. E. Hudson, A. J. Holder, K. M. Hawkins, P. R. Williams, and D. J. Curtis, "An enhanced rheometer inertia correction procedure (ERIC) for the study of gelling systems using combined motor-transducer rheometers," *Phys. Fluids* **29**(12), 121602 (2017).
- ⁷⁵M. Sentmanat, B. N. Wang, and G. H. McKinley, "Measuring the transient extensional rheology of polyethylene melts using the SER universal testing platform," *J. Rheol.* **49**(3), 585–606 (2005).
- ⁷⁶M. L. Sentmanat, "Miniature universal testing platform: From extensional melt rheology to solid-state deformation behavior," *Rheol. Acta* **43**(6), 657–669 (2004).
- ⁷⁷G. Nasif, R. Balachandrar, and R. M. Barron, "Supercritical flow characteristics in smooth open channels with different aspect ratios," *Phys. Fluids* **32**(10), 105102 (2020).
- ⁷⁸S. DeSouza and C. Segal, "Sub- and supercritical jet disintegration," *Phys. Fluids* **29**(4), 047107 (2017).
- ⁷⁹Q. Guo, J. Wang, C. B. Park, and M. Ohshima, "A microcellular foaming simulation system with a high pressure-drop rate," *Ind. Eng. Chem. Res.* **45**(18), 6153–6161 (2006).
- ⁸⁰C. B. Park, D. F. Baldwin, and N. P. Suh, "Effect of the pressure drop rate on cell nucleation in continuous processing of microcellular polymers," *Polym. Eng. Sci.* **35**(5), 432–440 (1995).
- ⁸¹H. Zuo, F. Javadpour, S. Deng, and H. Li, "Liquid slippage on rough hydrophobic surfaces with and without entrapped bubbles," *Phys. Fluids* **32**(8), 082003 (2020).
- ⁸²Y. Sato *et al.*, "Pressure-volume-temperature behavior of polylactide, poly(butylene succinate), and poly(butylene succinate-co-adipate)," *Polym. Eng. Sci.* **40**(12), 2602–2609 (2000).
- ⁸³G. T. Dee and D. J. Walsh, "Equations of state for polymer liquids," *Macromolecules* **21**(3), 811–815 (1988).
- ⁸⁴G. T. Dee and D. J. Walsh, "A modified cell model equation of state for polymer liquids," *Macromolecules* **21**(3), 815–817 (1988).
- ⁸⁵A. K. Mehrjerdi, T. Bashir, and M. Skrifvars, "Melt rheology and extrudate swell properties of talc filled polyethylene compounds," *Heliyon* **6**(5), e04060 (2020).
- ⁸⁶D. Xu, K. Yu, K. Qian, and C. B. Park, "Foaming behavior of microcellular poly(lactic acid)/TPU composites in supercritical CO₂," *J. Thermoplast. Compos. Mater.* **31**(1), 61–78 (2018).
- ⁸⁷V. Kumar and N. P. Suh, "A process for making microcellular thermoplastic parts," *Polym. Eng. Sci.* **30**(20), 1323–1329 (1990).
- ⁸⁸G. Finotello, J. T. Padding, N. G. Deen, A. Jongsma, F. Innings, and J. A. M. Kuipers, "Effect of viscosity on droplet-droplet collisional interaction," *Phys. Fluids* **29**(6), 067102 (2017).
- ⁸⁹T. Dong, W. H. Weheliye, P. Chausset, and P. Angeli, "An experimental study on the drop/interface partial coalescence with surfactants," *Phys. Fluids* **29** (10), 102101 (2017).
- ⁹⁰N. Barai and N. Mandal, "Breakup modes of fluid drops in confined shear flows," *Phys. Fluids* **28**(7), 073302 (2016).
- ⁹¹K. Feigl, A. Baniabedlruhman, F. X. Tanner, and E. J. Windhab, "Numerical simulations of the breakup of emulsion droplets inside a spraying nozzle," *Phys. Fluids* **28**(12), 123103 (2016).
- ⁹²I. Cuellar, P. D. Ravazzoli, J. A. Diez, and A. G. González, "Drop pattern resulting from the breakup of a bidimensional grid of liquid filaments," *Phys. Fluids* **29**(10), 102103 (2017).
- ⁹³S. Jain, M. Misra, A. K. Mohanty, and A. K. Ghosh, "Thermal, mechanical and rheological behavior of poly(lactic acid)/talc composites," *J. Polym. Environ.* **20**(4), 1027–1037 (2012).
- ⁹⁴M. Derakhshandeh, A. K. Doufas, and S. G. Hatzikiriakos, "Quiescent and shear-induced crystallization of polypropylenes," *Rheol. Acta* **53**(7), 519–535 (2014).

- ⁹⁵J. S. Tiang and J. M. Dealy, "Shear-induced crystallization of isotactic polypropylene studied by simultaneous light intensity and rheological measurements," *Polym. Eng. Sci.* **52**(4), 835–848 (2012).
- ⁹⁶M. Nofar, A. Tabatabaei, A. Ameli, and C. B. Park, "Comparison of melting and crystallization behaviors of polylactide under high-pressure CO₂, N₂, and He," *Polymer* **54**(23), 6471–6478 (2013).
- ⁹⁷J. R. Dorgan, J. S. Williams, and D. N. Lewis, "Melt rheology of poly(lactic acid): Entanglement and chain architecture effects," *J. Rheol.* **43**(5), 1141–1155 (1999).
- ⁹⁸M. Nofar, W. Zhu, C. B. Park, and J. Randall, "Crystallization kinetics of linear and long-chain-branched polylactide," *Ind. Eng. Chem. Res.* **50**(24), 13789–13798 (2011).
- ⁹⁹S. Saeidlou, M. A. Huneault, H. Li, and C. B. Park, "Poly(lactic acid) stereo-complex formation: Application to PLA rheological property modification," *J. Appl. Polym. Sci.* **131**(22), 41073 (2014).
- ¹⁰⁰T. S. Stephens, H. H. Winter, and M. Gottlieb, "The steady shear viscosity of filled polymeric liquids described by a linear superposition of two relaxation mechanisms," *Rheol. Acta* **27**(3), 263–272 (1988).
- ¹⁰¹D. C. Goel, "Effect of polymeric additives on the rheological properties of talc-filled polypropylene," *Polym. Eng. Sci.* **20**(3), 198–201 (1980).
- ¹⁰²M. M. Reddy and A. Singh, "Shear-induced particle migration and size segregation in bidisperse suspension flowing through symmetric T-shaped channel," *Phys. Fluids* **31**(5), 053305 (2019).
- ¹⁰³B. Chun, I. Kwon, H. W. Jung, and J. C. Hyun, "Lattice Boltzmann simulation of shear-induced particle migration in plane Couette–Poiseuille flow: Local ordering of suspension," *Phys. Fluids* **29**(12), 121605 (2017).
- ¹⁰⁴G. A. Roure and F. R. Cunha, "Hydrodynamic dispersion and aggregation induced by shear in non-Brownian magnetic suspensions," *Phys. Fluids* **30**(12), 122002 (2018).
- ¹⁰⁵S. Joung, M. Song, and D. Kim, "Synthetic capsule breakup in simple shear flow," *Phys. Fluids* **32**(11), 113603 (2020).
- ¹⁰⁶B. Rotenberg, A. J. Patel, and D. Chandler, "Molecular explanation for why talc surfaces can be both hydrophilic and hydrophobic," *J. Am. Chem. Soc.* **133**(50), 20521–20527 (2011).
- ¹⁰⁷C. Charnay, S. Lagerge, and S. Partyka, "Assessment of the surface heterogeneity of talc materials," *J. Colloid Interface Sci.* **233**(2), 250–258 (2001).
- ¹⁰⁸M. Ebrahimi, V. K. Konaganti, and S. G. Hatzikirakos, "Dynamic slip of polydisperse linear polymers using partitioned plate," *Phys. Fluids* **30**(3), 030601 (2018).
- ¹⁰⁹F. Yeganehdoust, R. Attarzadeh, A. Dolatabadi, and I. Karimfazli, "A comparison of bioinspired slippery and superhydrophobic surfaces: Micro-droplet impact," *Phys. Fluids* **33**(2), 022105 (2021).
- ¹¹⁰M. Najm and S. G. Hatzikirakos, "Flow-induced fractionation effects on slip of polydisperse polymer melts," *Phys. Fluids* **32**(7), 073109 (2020).
- ¹¹¹H. E. Park, S. T. Lim, F. Smillo, J. M. Dealy, and C. G. Robertson, "Wall slip and spurt flow of polybutadiene," *J. Rheol.* **52**(5), 1201–1239 (2008).
- ¹¹²H. E. Park, P. C. Lee, and C. W. Macosko, "Polymer-polymer interfacial slip by direct visualization and by stress reduction," *J. Rheol.* **54**(6), 1207–1218 (2010).
- ¹¹³A. U. Oza and D. C. Venerus, "The dynamics of parallel-plate and cone-plate flows," *Phys. Fluids* **33**(2), 023102 (2021).
- ¹¹⁴T. F. Lamer, B. R. Thomas, D. J. Curtis, N. Badiei, P. R. Williams, and K. Hawkins, "The application of large amplitude oscillatory stress in a study of fully formed fibrin clots," *Phys. Fluids* **29**(12), 121606 (2017).
- ¹¹⁵J.-E. Bae and K. S. Cho, "Analytical studies on the LAOS behaviors of some popularly used viscoelastic constitutive equations with a new insight on stress decomposition of normal stresses," *Phys. Fluids* **29**(9), 093103 (2017).
- ¹¹⁶M. A. Kanso, L. Jbara, A. J. Giacomini, C. Saengow, and P. H. Gilbert, "Order in polymeric liquids under oscillatory shear flow," *Phys. Fluids* **31**(3), 033103 (2019).
- ¹¹⁷J.-W. Song, M.-C. Ma, and L.-W. Fan, "Understanding the temperature dependence of contact angles of water on a smooth hydrophobic surface under pressurized conditions: An experimental study," *Langmuir* **36**(32), 9586–9595 (2020).
- ¹¹⁸K. Khechiba, M. Mamou, M. Hachemi, N. Delenda, and R. Rebhi, "Effect of Carreau–Yasuda rheological parameters on subcritical Lapwood convection in horizontal porous cavity saturated by shear-thinning fluid," *Phys. Fluids* **29**(6), 063101 (2017).
- ¹¹⁹H. E. Park, J. Dealy, and H. Münstedt, "Influence of long-chain branching on time-pressure and time-temperature shift factors for polystyrene and polyethylene," *Rheol. Acta* **46**(1), 153–159 (2006).
- ¹²⁰M. Gahleitner, "Melt rheology of polyolefins," *Prog. Polym. Sci.* **26**(6), 895–944 (2001).
- ¹²¹N. Topic *et al.*, "Effect of particle size ratio on shear-induced onset of particle motion at low particle Reynolds numbers: From high shielding to roughness," *Phys. Fluids* **31**(6), 063305 (2019).
- ¹²²L. Lombardi and D. Tammaro, "Effect of polymer swell in extrusion foaming of low-density polyethylene," *Phys. Fluids* **33**(3), 033104 (2021).
- ¹²³H. Münstedt, "New universal extensional rheometer for polymer melts. Measurements on a polystyrene sample," *J. Rheol.* **23**(4), 421–436 (1979).
- ¹²⁴J. Meissner and J. Hostettler, "A new elongational rheometer for polymer melts and other highly viscoelastic liquids," *Rheol. Acta* **33**(1), 1–21 (1994).
- ¹²⁵B. Li, W. Yu, X. Cao, and Q. Chen, "Horizontal extensional rheometry (HER) for low viscosity polymer melts," *J. Rheol.* **64**(1), 177–190 (2020).
- ¹²⁶A. Vázquez-Quesada and M. Ellero, "SPH modeling and simulation of spherical particles interacting in a viscoelastic matrix," *Phys. Fluids* **29**(12), 121609 (2017).
- ¹²⁷S. Das, S. Mandal, S. K. Som, and S. Chakraborty, "Effect of interfacial slip on the deformation of a viscoelastic drop in uniaxial extensional flow field," *Phys. Fluids* **29**(3), 032105 (2017).
- ¹²⁸E. S. Kim, H. E. Park, and P. C. Lee, "In situ shrinking fibers enhance strain hardening and foamability of linear polymers," *Polymer* **136**, 1–5 (2018).
- ¹²⁹M. S. Huda, L. T. Drzal, A. K. Mohanty, and M. Misra, "The effect of silane treated- and untreated-talc on the mechanical and physico-mechanical properties of poly(lactic acid)/newspaper fibers/talc hybrid composites," *Composites, Part B* **38**(3), 367–379 (2007).
- ¹³⁰C. G. Skamniotis, M. Elliott, and M. N. Charalambides, "On modeling the large strain fracture behaviour of soft viscous foods," *Phys. Fluids* **29**(12), 121610 (2017).
- ¹³¹N. O. Rojas, "Air bubble propagation mechanism in a rectangular elasto-rigid channel," *Phys. Fluids* **33**(3), 032103 (2021).
- ¹³²S. N. Leung, C. B. Park, D. Xu, H. Li, and R. G. Fenton, "Computer simulation of bubble-growth phenomena in foaming," *Ind. Eng. Chem. Res.* **45**(23), 7823–7831 (2006).
- ¹³³P. Buahom and S. Areerat, "The estimation of cell density in isotropic micro-cellular polymeric foams using the critical bubble lattice," *J. Cell. Plast.* **47**(2), 133–152 (2011).
- ¹³⁴M. Nofar and C. B. Park, "Heterogeneous cell nucleation mechanisms in polylactide foaming," in *Biofoams*, edited by S. Iannace and C. B. Park (CRC Press, Boca Raton, 2015).
- ¹³⁵A. Ameli, D. Jahani, M. Nofar, P. U. Jung, and C. B. Park, "Development of high void fraction polylactide composite foams using injection molding: Mechanical and thermal insulation properties," *Compos. Sci. Technol.* **90**, 88–95 (2014).
- ¹³⁶A. Ameli, M. Nofar, D. Jahani, G. Rizvi, and C. B. Park, "Development of high void fraction polylactide composite foams using injection molding: Crystallization and foaming behaviors," *Chem. Eng. J.* **262**, 78–87 (2015).
- ¹³⁷H. E. Naguib, C. B. Park, and P. C. Lee, "Effect of talc content on the volume expansion ratio of extruded PP foams," *J. Cell. Plast.* **39**(6), 499–511 (2003).
- ¹³⁸S. M. Ovais, K. A. Kemenov, and R. S. Miller, "Direct numerical simulation of supercritical oxy-methane mixing layers with CO₂ substituted counterparts," *Phys. Fluids* **33**(3), 035115 (2021).
- ¹³⁹M. Nofar, A. Ameli, and C. B. Park, "A novel technology to manufacture biodegradable polylactide bead foam products," *Mater. Des.* **83**, 413–421 (2015).
- ¹⁴⁰L. F. McInerney, N. Kao, and S. N. Bhattacharya, "Melt strength and extensibility of talc-filled polypropylene," *Polym. Eng. Sci.* **43**(12), 1821–1829 (2003).
- ¹⁴¹W. Kaewmesri, P. C. Lee, C. B. Park, and J. Pumchusak, "Effects of CO₂ and talc contents on foaming behavior of recyclable high-melt-strength PP," *J. Cell. Plast.* **42**(5), 405–428 (2006).
- ¹⁴²D. Jahani, A. Ameli, P. U. Jung, M. R. Barzegari, C. B. Park, and H. Naguib, "Open-cell cavity-integrated injection-molded acoustic polypropylene foams," *Mater. Des.* **53**, 20–28 (2014).

- ¹⁴³D. Kohlhoff and M. Ohshima, "Open cell microcellular foams of polylactic acid (PLA)-based blends with semi-interpenetrating polymer networks," *Macromol. Mater. Eng.* **296**(8), 770–777 (2011).
- ¹⁴⁴H. Li *et al.*, "Evaluation of oil production potential in fractured porous media," *Phys. Fluids* **31**(5), 052104 (2019).
- ¹⁴⁵B. Li, G. Zhao, G. Wang, L. Zhang, J. Gong, and Z. Shi, "Biodegradable PLA/PBS open-cell foam fabricated by supercritical CO₂ foaming for selective oil-adsorption," *Sep. Purif. Technol.* **257**, 117949 (2021).
- ¹⁴⁶O. Maalal, M. Prat, and D. Lasseux, "Pore network model of drying with Kelvin effect," *Phys. Fluids* **33**(2), 027103 (2021).
- ¹⁴⁷C. McIlroy, "A fundamental rule: Determining the importance of flow prior to polymer crystallization," *Phys. Fluids* **31**(11), 113103 (2019).
- ¹⁴⁸Y. Lin, Y. Wang, Z. Weng, D. Pan, and J. Chen, "Air bubbles play a role in shear thinning of non-colloidal suspensions," *Phys. Fluids* **33**(1), 011702 (2021).
- ¹⁴⁹M. Agrawal, A. Gaurav, B. Karri, and K. C. Sahu, "An experimental study of two identical air bubbles rising side-by-side in water," *Phys. Fluids* **33**(3), 032106 (2021).
- ¹⁵⁰S. Li, A. M. Zhang, R. Han, and Y. Q. Liu, "Experimental and numerical study on bubble-sphere interaction near a rigid wall," *Phys. Fluids* **29**(9), 092102 (2017).
- ¹⁵¹G. Charalampous and Y. Hardalupas, "Collisions of droplets on spherical particles," *Phys. Fluids* **29**(10), 103305 (2017).
- ¹⁵²S. A. Banitabaei and A. Amirfazli, "Droplet impact onto a solid sphere: Effect of wettability and impact velocity," *Phys. Fluids* **29**(6), 062111 (2017).
- ¹⁵³S. Chen and V. Bertola, "Drop impact on spherical soft surfaces," *Phys. Fluids* **29**(8), 082106 (2017).
- ¹⁵⁴L. T. Liu, X. L. Yao, A. M. Zhang, and Y. Y. Chen, "Numerical analysis of the jet stage of bubble near a solid wall using a front tracking method," *Phys. Fluids* **29**(1), 012105 (2017).
- ¹⁵⁵P. Koukouvini, M. Gavaises, O. Supponen, and M. Farhat, "Simulation of bubble expansion and collapse in the vicinity of a free surface," *Phys. Fluids* **28**(5), 052103 (2016).
- ¹⁵⁶V. Kumar, M. Kumawat, A. Srivastava, and S. Karagadde, "Mechanism of flow reversal during solidification of an anomalous liquid," *Phys. Fluids* **29**(12), 123603 (2017).
- ¹⁵⁷F. Duan, L. Zhao, X. Chen, and Q. Zhou, "Fluid-particle drag and particle-particle drag in low-Reynolds-number bidisperse gas-solid suspensions," *Phys. Fluids* **32**(11), 113311 (2020).
- ¹⁵⁸P. M. Vinze, A. Choudhary, and S. Pushpavanam, "Motion of an active particle in a linear concentration gradient," *Phys. Fluids* **33**(3), 032011 (2021).
- ¹⁵⁹R. E. Swaney and R. B. Bird, "Transport phenomena and thermodynamics: Multicomponent mixtures," *Phys. Fluids* **31**(2), 021202 (2019).
- ¹⁶⁰K. Pandey, D. Prabhakaran, and S. Basu, "Review of transport processes and particle self-assembly in acoustically levitated nanofluid droplets," *Phys. Fluids* **31**(11), 112102 (2019).
- ¹⁶¹S. H. Mahmood, A. Ameli, N. Hossieny, and C. B. Park, "The interfacial tension of molten polylactide in supercritical carbon dioxide," *J. Chem. Thermodyn.* **75**, 69–76 (2014).
- ¹⁶²F. Y. Leong and D.-V. Le, "Droplet dynamics on viscoelastic soft substrate: Toward coalescence control," *Phys. Fluids* **32**(6), 062102 (2020).